

國立清華大學

National Tsing Hua University

博士論文

光與電雙功能矽場效應電晶體分子感測器

A Dual Function Electro-Optical Silicon Field-Effect

Transistor Molecular Sensor



系別 : 工程與系統科學系

學號 : 104011865

研究生 : Pradhana Jati Budhi Laksana

指導教授: 陳啟東博士 (Prof. Chii-Dong Chen)

張廖貴術博士 (Prof. Kuei-Shu Chang-Liao)

中華民國一百一十一年十一月

摘要

近年來，以場效應電晶體 (bio-FETs) 為基礎的生物傳感器因其獨特的特性、高靈敏度、良好的選擇性以及易於應用於便攜式電子設備中而受到人們矚目及興趣。在本實驗中，我們設計並展示了一種利用 FET 即時檢測分子之間相互作用的方法。在此方法中，利用 FET 傳感器電訊號和光訊號高靈敏度的獨特功能。使用場效應電晶體來檢測與抗體和抗原分子結合前後，分子電荷和光子吸收的訊號變化。採用固定在 FET 表面的酵素免疫分析法(ELISA) 夾層結構來檢測嗜中性白血球明膠酶相關脂質運載蛋白 (NGAL)。利用這種實驗技術，對 NGAL 靈敏度定量檢測，電訊號的檢測靈敏度達到 0.1 pg/mL，氧化 TMB 光吸收檢測具有 < 1 pg/mL 的靈敏度。接著我們研究了矽奈米線場效應電晶體 (bio-NW FET) 的生物感測器作為分子光吸收感測器的潛力。以槲皮素和銅 (Cu^{2+}) 離子為例，使用 opto-FET 方法檢測分子的相互作用，研究顯示波長為 450 nm 的光會被化合物所吸收，吸收量則取決於 Cu^{2+} 的濃度。對介於 0.1 μM 和 100 μM 之間的 Cu^{2+} 濃度進行化合物分子吸收的定量檢測，在優化後的系統電位參數下，分子對光的吸收量與銅離子濃度呈線性正比關係，結果顯示本研究使用的 opto-FET 方法所檢測到的光吸收度不亞於市面上常見的紫外-可見分光光度法，此外，我們證明此量測平台在生物傳感器的臨床應用中表現出色。

關鍵詞：分子吸收光譜，分子電荷，奈米矽線，生物感測器，場效應晶體管，ELISA，NGAL，比色法，金屬配合物。

Abstract

The biosensor based on field-effect transistors (bio-FETs) has have attracted great interest in recent years owing to their unique properties, high sensitivity, good selectivity, and easy integration into portable electronic devices. In this work, we propose and demonstrate a method that utilizes FETs for real-time detection of interactions between molecules. In this method, FET based sensors employ two unique functions, high charge sensitivity and high photon responsivity. We use the transistors to detect changes in molecular charge and photon absorption related with the binding of antibody and antigen molecules. We adopt an Enzyme-Linked Immunosorbent Assay (ELISA) sandwich structure immobilized on the FET surface to detect neutrophil gelatinase associated lipocalin (NGAL). Using this technique, we detect NGAL quantitatively with a sensitivity of 0.1 pg/mL and < 1 pg/mL based on charge sensing and oxidized TMB absorption detection, respectively.

Next, we explored the potential of applying biosensors based on silicon nanowire field-effect transistors (bio-NW FETs) as molecular absorption sensors. Using quercetin and Copper (Cu^{2+}) ion as an example, we demonstrated the use of an opto-FET approach for the detection of molecular interactions. We found that photons with wavelengths of 450 nm were absorbed by the molecular complex, with the absorbance level depending on the Cu^{2+} concentration. Quantitative detection of the molecular absorption of metal complexes was performed for Cu^{2+} concentrations ranging between 0.1 μM and 100 μM , in which the photon response increased linearly with the copper concentration under optimized bias parameters. Our opto-FET approach showed a comparable absorbance with that of a commercial ultraviolet-visible spectrophotometry. Furthermore, we show that this platform performs great for diagnostic applications of biosensors.

Keywords: Molecular charge, molecular absorption, silicon nanowire, biosensor, field-effect transistor, ELISA, NGAL, colorimetric, metal complexes.



Acknowledgement

“Life is a journey. Enjoy and face every turn and trip. Keep moving, focusing, and enjoying every step along the way. All those small and big steps will lead to your destination. Stay patient and trust yourself. And you will find a reward for your journey.

“The quote is easy-peasy to say but challenging to do. During my doctoral study there were many events that made me both weak and strong, but I have to face, find solutions, and not avoid it. It is the only way to make us advance in progress, even just a little.

This thesis is submitted as a partial fulfilment of the requirements for the TIGP-NTHU ESS doctoral degree and is the results of research carried out at the Biosensor group of Quela Lab of Professor Chii-Dong Chen. It would not have been possible without the support and encouragement of many people including my family, friends and group members.

First, I would like to express my sincere gratitude to my supervisor, Professor Chii-Dong Chen for his support, guidance and council while conducting this study. I thank him for his guidance, innovative idea, critical opinion, and training throughout my PhD studies that will continue to be of value going forward. It is my honor to work in Prof. Chen’s group where I have been taught how to think about questions logically, do things reliably, and present results clearly. I would like to express my gratitude to biosensor and quantum electronic lab members, senior and junior, for their kind help during my PhD study.

I am particularly grateful to Prof. Kuei-Shu Chang-Liao, my co-advisor from NTHU, for his continues help, support and fruitful discussions. I would like to extend my thanks to the thesis committee members: Prof. Li-Chu Tsai, Prof. Yit-Tsong Chen, and Prof. Chia-Fu Chou for their valuable times and comments.

I would like to acknowledge Nano-TIGP and Institute of Physics (IoP) at Academia Sinica for their support throughout my PhD studies. Special thanks go to Ms. Flora, Nano-TIGP program assistant, who sincerely helped me a lot. I also thank the staff of IoP for all support.

My sincere gratitude to Molsentech (矽基分子電測科技股份有限公司) company, Dr. Chia-Jung Chu and Dr. Ming-Chou Lin and colleague for the discussion, I can see this start-up company will grow-up as a good company. For Ke Jun-Chuan, thank you for helping me in many things. I would like to thank the Indonesian Government especially Kota Semarang and Provinsi Jawa Tengah for the continuous support.

I very much appreciate the love, support, encouragement and all the efforts from my parents, my family and my friends. Finally, I would like to deeply thank my lovely and wonderful wife Dany Perwita Sari and my son Lionel Nada Laksana for accompanying during this journey in Taipei, Taiwan, we always love this city.

Above all, thank you Jesus. This achievement was made possible by you. This is all for you Lord God, I lift everything up to honor you. I love you and I trust you. To God be the Glory.

Table of Contents

摘要.....	i
Abstract.....	ii
Acknowledgement	iv
Table of Contents	vi
List of Figures.....	viii
List of Table	xiii
Chapter 1 Introduction.....	1
Chapter 2 Background, Principles, and Concepts	4
2.1. Biosensor.....	4
2.2. Silicon Nanowire Field-Effect Transistor	5
2.2.1. Working Principle of Silicon Nanowire-based Device.....	7
2.2.2. Si-NW Bio-FET.....	9
2.2.3. Photosensitive Si-NW Bio-FET.....	13
2.3. Debye Length Screening	14
2.4. Surface Modification and Functionalization of Silicon Oxide	15
2.5. Enzyme-linked Immunosorbent Assay (ELISA) and NGAL	17
Chapter 3 Device Fabrication and Measurement Technique.....	21
3.1. Fabrication of Si-NW Bio-FET	21
3.2. Fluidic Channel.....	23
3.3. Measurement System	25

3.4. Procedure of Surface Modification and Functionalization of Silicon Oxide.....	27
3.5. Procedure of Molecular Charge Detection	29
3.6. Procedure of Molecular Absorption Detection.....	29
3.7. Materials	31
Chapter 4 Detection of Molecular Charge and Molecular Absorption.....	32
4.1. Absorption Spectra of HRP Redox Reaction with TMB.....	32
4.2. Device Characteristics of Si-NW Bio-FET.....	33
4.3. Photosensitive Si-NW Bio-FET.....	34
4.4. Surface Modification of Si-NW Bio-FET.....	37
4.5. Detection of Molecular Charge.....	40
4.6. Detection of Molecular Absorption.....	43
4.7. Detection of Quercetin - Cu ²⁺ complexes using bio-FET as photodetector	45
Chapter 5 Conclusions.....	52
References.....	53
Appendix.....	60



List of Figures

Figure 2.1.	Basic scheme of a biosensor.....	5
Figure 2.2.	Schematic illustration of silicon nanowire field-effect transistor	7
Figure 2.3.	Schematic illustration of Si-NW FET (a) accumulation mode and (b) inversion mode.	8
Figure 2.4.	Structural evolution of functional gate field-effect transistors.....	9
Figure 2.5.	Schematic illustration of (a). a typical field-effect transistor biosensor and (b). transfer characteristics of n-type field-effect transistor for more positive charge accumulated in the surface.	10
Figure 2.6.	Illustration of cross-section of bio-FET during molecular interaction.....	12
Figure 2.7.	Illustration of the photoelectric process in a semiconductor material. A photon is absorbed when it has enough energy to excite an electron from the valence band to the conduction band, leaving behind a hole.	13
Figure 2.8.	Mechanism of photocurrent generation in Si-NW FET... ..	14
Figure 2.9.	Molecular structure of (a) APTES, (b) TPMS, (c) MPTES, and (d) GOPTES. (a-d from website of Sigma-Aldrich) (e) Schematic of fabrication of silane molecules monolayer.....	16
Figure 2.10.	Molecular arrangement of APTES connecting inorganic materials through silanization reaction. There are five different molecular structures in the above figure, of which (a) to (d) are all covalent structures composed of surface hydroxyl groups and silanes, and (e) is the surface hydrogen bonding reaction between amine groups and hydroxyl groups.	17
Figure 2.11.	Schematic diagram of antibodies. Antibodies have antigen-binding sites that bind to antigens in their structure, are highly specific, and can recognize specific substrates.	18
Figure 2.12.	Schematic diagram of common ELISA method using HRP enzyme and TMB substrate: (a) direct ELISA method, (b) Indirect method, (c) The	

	sandwich method. The TMB oxidase is the final step of ELISA which produce the colored solution.	20
Figure 3.1.	Structure of SOI wafer. The thicknesses of top Si layer, buried silicon dioxide layer are 200 nm, 400 nm and 525 μm	21
Figure 3.2.	The SEM image of the FET device with channel length, width, and thickness of the wire equal to 3 μm , 200 nm, and 100 nm, respectively.	19
Figure 3.3.	(a) fluidic channel mold, (b) fluidic channel slabs, (c) sensor assembly.	23
Figure 3.4.	The setup of fluidic channel in sensor assembly (a) Bio-FET and (b) Opto-FET. In bio-FET, the sample solution is exposed to the surface of sensing region. And in opto-FET, the sample solution is unexposed to the surface of sensing region, FET as a photodetector.	24
Figure 3.5.	Amplifier circuit for signal amplification.	25
Figure 3.6.	The deployment and photographs of the measurement system.....	26
Figure 3.7.	Molecule structural illustration of the probe molecules surface modification.	27
Figure 3.8.	The illustration of an ELISA sandwich structure steps in Si-NW surface. Primary antibody (blue), NGAL (yellow) represents antigen, biotinylated secondary antibody (brown), conjugated HRP-streptavidin (red), and TMB (blue).	29
Figure 4.1.	The UV-Vis absorption spectra of TMB oxidation products. Experiments were carried out using 100 μL TMB and 20 μL HRP in the phosphate buffered saline solution at pH at 7.4 and temperature at 25 $^{\circ}\text{C}$. The spectrophotometer was swept from 200 to 1000 nm and there were 20 times measurement with interval of 2 minutes. (inset) Absorption evolution of TMB oxidation product at wavelength of 372 (orange), 650 (blue), and 910 (grey) nm.....	32
Figure 4.2.	Basic characterization of FET: (a) Output characteristics of the silicon FET sensor and (b) pH sensitivity response of the FET device ranging from pH 4 to pH 9. The bias condition VDS 0.5 V, VLG -1 V to 1.5 V, and VBG was kept constant at 0 V.....	33

- Figure 4.3. The photoresponse of the bio-FET in air. In (a), illumination current (red) and dark current (black) of wavelengths from 300 to 1100 nm. (b) The photocurrent, is expressed as the absolute value of subtraction the illumination current from dark current. The spectrum is taken with drain voltage (VDS) set at 0.5 V and back-gate voltage (VBG) set at 0 V.....34
- Figure 4.4. Photo-absorption spectrum of the oxidized TMB measured using a measurement setups shown in figure 3.5a (a) The photoresponse of FET in 1x PBS (green), and with HRP-surface modification (red), and after adding in TMB to react with the surface HRP (blue). (b) The result of a subtraction of “HRP” from “HRP+TMB” curve in (a). (c) A comparison between the oxidized TMB photo absorption spectrums measured using a FET (red) and a commercial spectrophotometer (black).35
- Figure 4.5. In (a) IDS-VBG response of the FET under various levels of light illumination: dark (black), 4.6 (green), 7.6 (brown), 14.8 (blue), 20.8 (red) and 109 (orange) $\mu\text{W}/\text{cm}^2$ with bias condition VDS 0.5 V, VBG -5 V to 5 V, and VLG was kept constant at 0V. The current at all back-gate voltage decreases with increasing light intensity. In (b) red dots are measured photocurrent, and the black curve is the power-law fitting. The inset shows on/off photocurrent under 1 $\mu\text{W}/\text{cm}^2$ light intensity. Photocurrent increases sub linearly and follows power-law dependence for light intensity below 11 $\mu\text{W}/\text{cm}^2$37
- Figure 4.6. IDS-VBG curve bare chip (blue) and after APTES modification (red) in air. the blue arrow indicate that the curve shift left after surface modification.32
- Figure 4.7. Test the Ninhydrin solution using silicon chip. (a) blank silicon chip and (b) APTES modified silicon chip. A ninhydrin solution is dropped into both chip blank and APTES modified silicon chip and the heated on 100 °C. The APTES modified chip showing blue-purple color, which indicated that ninhydrin would undergo chelation reaction with primary amine.38
- Figure 4.8. (a) IDS-VBG of modified molecules in buffer solution. After APTES modification (red), after glutaraldehyde (green), after ethanolamine

	blocking (cyan) and after Antibody (orange). (b) the VBG shift of each surface functionalization.	39
Figure 4.9.	The real-time of bio-FET response to different concentrations of NGAL ranging from 0.1 to 50 pg/mL.	40
Figure 4.10.	The measurement of drain current of bio-FET for several NGAL concentrations (a) ranging from 0.1 to 50 pg/mL with a high concentration of BSA as a control experiment for selectivity test and (b) drain current (%) as the function of log NGAL concentration.	41
Figure 4.11.	The bio-FET current as a function of the back gate voltage taken before (black) and after (red) the measurement shown in Figure 4.9.	42
Figure 4.12.	Real-time measurement of increasing oxidized TMB concentration in response to various NGAL concentrations. Transmittance traces correspond to NGAL concentrations without NGAL as control (black), 1 pg/mL (purple), 10 pg/mL (green), 25 pg/mL (red), and 50 pg/mL (blue). The experimental data are presented as colored dots, and the fittings are shown as thick solid curves with the corresponding colors. From saturation transmittance and reaction time extracted from exponential fitting $T(\text{min}) = (100 - \beta) \exp((-t)/\alpha) + \beta$, one can figure out the level-off value (β) and the characteristic reaction time (α). These are presented in (b) and (c), respectively.	43
Figure 4.13.	The color evolution of oxidized TMB for 50 pg/mL NGAL at different time in minutes.	45
Figure 4.14.	(a) UV-Vis absorption spectra of quercetin and various concentrations of Cu^{2+} in 1X PBS showing two peaks at 380 nm and 450 nm, and (b) the absorbance as a function of Cu^{2+} concentration at 450 nm.	47
Figure 4.15.	The visual change of quercetin and Cu^{2+} complexes. The pure quercetin (left) followed by mixing of quercetin and different Cu^{2+} concentrations ranging from 1 to 100 μM	48
Figure 4.16.	(a) The photocurrent at a wavelength of 450 nm plotted as functions of VBG and light intensities, for VDS at 0.2 V, 0.5 V, 1 V, 2 V, and 3 V. The color scale bar is shown on the right. (b) The photocurrent as a function of	

light intensity. It shows a linear dependence at $V_{DS} = 0.5$ V and $V_{BG} = 2.8$ V.49

Figure 4.17. Absorption measurement of quercetin– Cu^{2+} ion mixture for various Cu^{2+} concentrations ranging from 0.1 μM to 100 μM in three different concentrations of PBS solution. A 100 μM quercetin was used as a control sample.....50

Figure 4.18. A comparison between the absorbance achieved with a commercial UV–Vis spectrometer (dot-dashed lines) and our opto-FET system (solid lines) in (a) 0.01X (b) 0.1X, and (c) 1X PBS concentration. The evaluation was performed in V_{DS} at 0.5 V, V_{BG} at 2.8 V, a wavelength of 450 nm, and light intensity at 500 nWcm^{-2}51



List of Table

Table 3.1.	List of materials.....	31
Table 4.1.	Comparison our device with other method on NGAL detection	35



Chapter 1 Introduction

The incorporation of nanomaterials into device structures for biosensing applications has led to the development of new methods for signal transducers. A combination of nanomaterials such as nanoparticles, nanotubes, and nanowires with biological molecules, offers potential in developing sensor technology for molecular size scale detection of biomolecules, since biological molecules and nanomaterials are of comparable size. For instance, the molecular adsorption can induce cantilever deflection through its weight that resulting resonance frequency change, change the plasmon resonance in metallic nanostructures and modulate the electrical conductivity in nanowires. All these principles have been demonstrated to work as signal transduction mechanism in surface analysis and makes the sensor work through mechanical, optical, or electrical detection. Due to the fact that silicon serves as the foundational component of microelectronics, silicon nanowires are of particular importance. With its high abundance, moderate bandgap, and ease of fabrication, silicon has become the most suitable material for building powerful sensing devices. Silicon nanowires, which are one dimensional (1D) nanomaterials, have become one of the most promising sensing materials due to their surface area to volume ratio and high stability. Since introduced in 2001 by Lieber group as an electrical field based sensor, silicon nanowire field-effect transistors (Si-NW FET) have been demonstrated greatly for a wide-range of bio and chemical detections [1,2]. Si-NW FET has been shown excellent capability for the rapid, accurate, label-free and real-time detection such as virus [3], cancer-related biomarker [4], nucleic acids [5], cells [6,7] and proteins [8,9] and bacteria [10], makes Si-NW FET as promising practical biosensors for ultrasensitive clinical diagnostic tools (bio-FET). These detection limits are two orders of magnitude lower than those that have been reported with quantum dots and carbon nanotubes. Moreover, owing to their 1-D morphology and increased surface to volume ratio,

bio-FETs provide improved sensitivity as compared to planar FET devices. With its submicron ultimate feature size and mass-produced at a low cost, making them a good option for disposable biosensors, thanks to the advantage of the mature semiconductor manufacturing industry.

Bio-FET comprises three regions: source, drain, and a channel region. The channel region, which is covered with oxide, is exposed to an analyte solution and functionalized with probe molecules. The probe molecule is designed to interact specifically to certain target species in the analyte solution. The molecular charge changes upon the interaction between the target and probe molecules in the surface of the channel region. That charge-changing induces the conduction carrier inside the nanowires and changes the source-drain current.

It is common to keep the analyte in a high ionic strength solution to prevent the molecular structure from losing activity and binding affinity. [11-14]. Unfortunately, in high ionic strength solution, the Debye length, which is inversely proportional to the square root of ionic strength, is short. It is resulting in a smeared molecular charge being seen by the bio-FET sensors [15,16]. On the other hand, photon radiation effect towards the bio-FET induced conduction carriers in the channel region and change the source-drain current, which indicates that bio-FET can also function as an optical transducer [17]. This capability allows bio-FETs to be used as optical biosensors capable of detecting molecular binding-induced changes that occur during absorption, reflection, and emission. This issue regarding Debye screening length vis-à-vis FET charge sensors can be resolved.

In this dissertation, we explored two functions of bio-FET, namely charge sensing to detect molecular-charge and optical transduction to detect molecular absorption properties. [18] In the following of introduction, **Chapter 2**, we give a brief introduction to the Si-NW FET. This chapter describes how the Si-NW works as biosensor, how photon induced charge in Si-

NW, Debye length limitation and surface modification and functionalization of bio-FET and APTES. **Chapter 3** covers the experimental method to fabrication the device, the measurement system and fluidic channel, the electrical and optical characterization method, detection procedure and materials. **Chapter 4** investigates the detection of molecular charge and molecular absorption in our bio-FET. We followed the enzyme-linked immunosorbent assay (ELISA) technique as a proof of concept experiment to demonstrate bio-FET charges and photon capabilities. The neutrophil gelatinase-associated lipocalin (NGAL) [19] was selected as a target molecule for the illustration of the two functions. We also demonstrated the bio-FET as photodetector by utilize quercetin and copper (Cu^{2+}) ion as an example. [20] Finally, the bio-FET showed the good performance for molecular charge and molecular absorption. **Chapter 5** we summarize the dissertation.



Chapter 2 Background, Principles, and Concepts

Recently, there has been a gradual increase of companies based on biosensor technology around the world. In general, it can be said that biosensors have found an important place in our society as they aim to improve the quality of life in various regions and prevent the emergence of chronic diseases and pandemics. There are many tools and methodologies used as biosensors. In this chapter, the theoretical about biosensors and their components will be introduced in detail. The principle and concept of Si-NW FET as an analytical device also will be explained including the working principle and the properties.

2.1. Biosensor

The use of biosensors is ubiquitous these day in many fields, such as point-of-care monitoring of diseases, monitoring of treatments, environmental, food, forensics, and biomedical research. According to the IUPAC definition, a biosensor is defined as a device that uses specific biochemical reactions mediated by an isolated enzyme, immunosystems, tissues, organelles or whole cells to detect chemical compounds usually by electrical, thermal or optical signals [21]. Detection of corona virus (Covid-19) [3,22,23] and glucose [24] sensor are examples of sensors that is used day-to-day life. The global pandemic, the desire to improve the quality of life and rapid industrial developments are driving the demand for research and development of biosensors. The ideal biosensor is portable, user-friendly, sensitive, selective in any complex medium, inexpensive, and rapid in order to produce a measurable signal output [25]. However, such an ideal biosensor is far from reality despite of the massive progress made over the last decade.

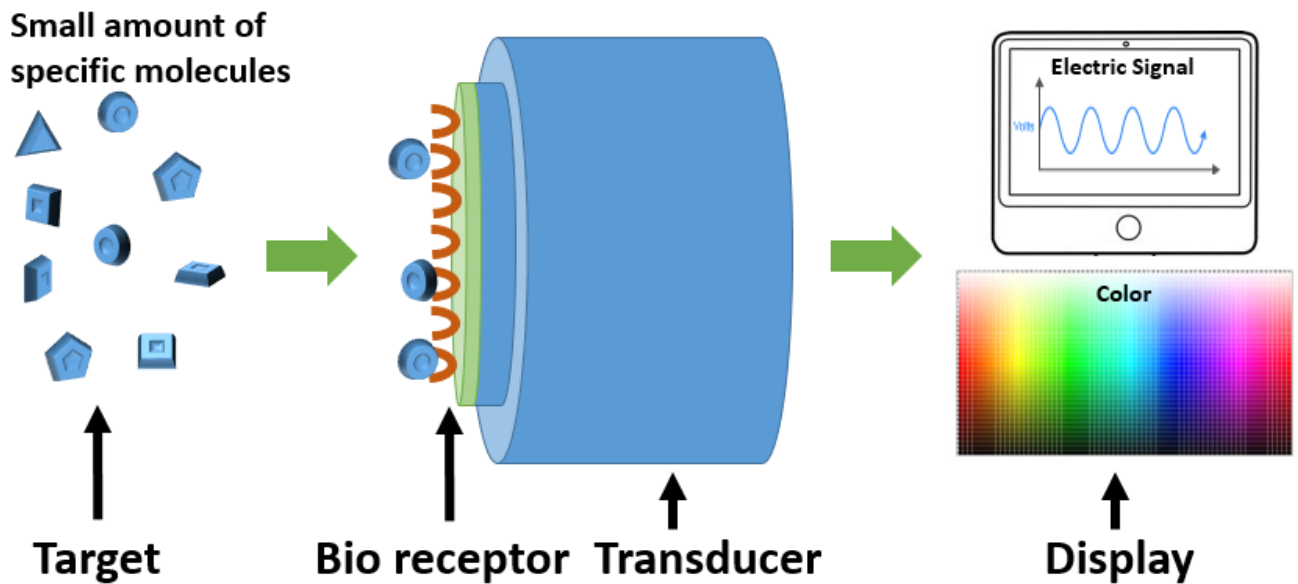


Figure 2.1. Basic scheme of a biosensor.

Generally, a biosensor comprises of three main parts as shown in **Figure 2.1**. These consist of a biological sensing element or receptor, transducer or physicochemical detector, and signal processing system. A biological sensing elements are used to react with the analyte of the interest such as antibodies, enzyme, nucleic acid, tissues, cell receptors, virus, microorganism and etc. The transducer transform the signal generated through the interaction of the biological sensing elements and the analyte of interest into another signal that can be more easily measured and quantified. The transducer is based on a mechanism for example optical, field-effect, electrochemical, electrochemiluminescence, and etc. The signal processing system involves in amplifying the signal and converting into a data processor that produce a measurable signal in the form of display, or color change. Based on the transducer, biosensors can be classified as electrochemical (field-effect transistor, impedance spectroscopy, etc.), optical (surface plasmon resonance, surface-enhanced raman scattering, UV-Vis, etc.), thermal, and mass (quartz crystal microbalance, piezoelectric, etc.).

2.2. Silicon Nanowire Field-Effect Transistor

Nanowires are nanostructures with diameters in the nanometer scale. The top-down [26] methods like photo-lithography and bottom-up [27] methods like vapor and liquid phase syntheses are basic methods for nanowires that have been mature in advance semiconductor manufacturing industry, especially for silicon material. Silicon nanowires (Si-NWs) are famous nanomaterials because of their excellent mechanical and electrical characteristics. The field effect action can control the conductivity of the Si-NWs, thanks to the semiconductor nature of silicon [28]. Due to this reason, there is possible usage of Si-NWs for the next generation of advanced sensors and field-effect transistor.

In an advanced fabrication process, the semiconductor properties of Si-NW be effectively controlled. For instance, the doping type and concentration directly affects the charge carrier of electron or hole density, and thermal annealing can enhance the carrier mobility of Si-NW [29]. Moreover, the nanowire structure represents the minimum dimension for electrical conductivity. Compared to devices prepared from carbon nanotubes and organic materials like from conducting polymers, Si-NW devices are more suitable with large scale fabrication and integration process, in addition the devices can be mass produced at low cost [30]. In terms of the fundamental of biosensor, Si-NWs are easily to produced, high yielded, and better understood than devices base on polymer nanowires. Moreover, the capability to chemically modify the surface of Si-NW enables the wide application of biosensors [31].

For the fabrication process of the Si-NW, there are two methods, bottom-up and top-down method. In the bottom-up method, the nanowire can be grown from reactive precursors, using nanoparticles or nanostructured template to build the desired nanostructured through self-assembly. This method typically required the transfer and deposition of the nanowire into a substrate, followed by the fabrication of the contact pads. In the top-down method, the nanowire can be built by transfer pattern using photo-lithography or e-beam lithography, then

reducing the dimension with reactive ion etching and doping by ion implantation, followed by deposition and etching of the contact pad. Recently, the top-down method is growing popularly for the research and development. It mainly because it has advantages of the ease, reproducibility, and reliability of the device designing and the integration possibilities to CMOS technology, especially with the fully depleted SOI wafer.

2.2.1. Working Principle of Silicon Nanowire-based Device.

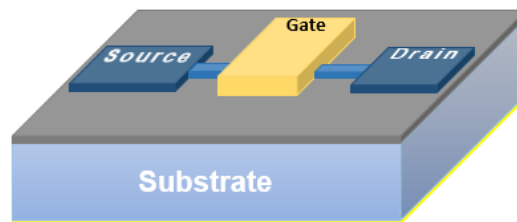


Figure 2.2. Schematic illustration of silicon nanowire field-effect transistor

The Si-NW FET device comprises of source, drain, and gate electrode. The function of the source and drain electrodes is to bridge the semiconductor channel made of Si-NW, and the gate electrode is to modulate channel conductivity. The gate is separated from the channel by a dielectric material, generally SiO_2 or Si_3N_4 . For the device made on silicon on insulator wafer, it will have front- and back-gate for double gate FET. The voltage applied to the gate electrode controls the effective cross section area of the conducting channel in the nanowire. The channel of an FET is doped to produce either an n-type or a p-type semiconductor. The drain and source is commonly a heavily-doped doping of n-type or p-type to provide a low-resistivity connection and good contact to metal electrode. With these type of doping, the device can possibly be forming an accumulation mode and inversion mode transistor. The accumulation mode transistor has configuration across the device like $\text{p}^+\text{-p-p}^+$ or $\text{n}^+\text{-n-n}^+$, and the inversion mode has configuration like $\text{p}^+\text{-n-p}^+$ or $\text{n}^+\text{-p-n}^+$. as illustrated in **Figure 2.3**. When the source-drain voltage applied in the device, in accumulation mode, as the doping across the device is in the

same polarity, the energy barrier between channel region and source/drain is small, and thus the V_{DS} is sufficient for the current flow without biasing the gate voltage. In other words, the accumulation mode FETs are normally-on devices and thus the current level is high at V_G at 0. The device is normally on. In contrast, the current flow is typically blocked in an equilibrium state at V_G at 0 in an inversion mode FET due to the junction between the channel and source-drain. However, gate potential alters conduction- and valence-band bending which modulate the charge carrier distribution on each band. A sufficient voltage induces the charge carriers which can flow between source and drain. As a result, the surface potential modulation of the silicon channel controls the current flows and the switching functionality determined by the threshold voltage (V_{TH}).

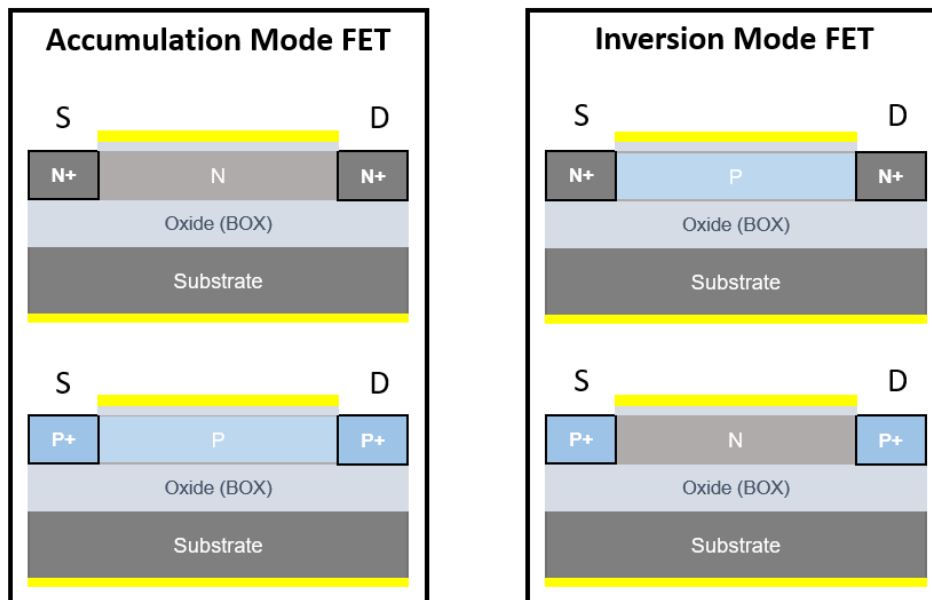


Figure 2.3. Schematic illustration of Si-NW FET (a) accumulation mode and (b) inversion mode.

For a constant source-drain voltage, the amount of current flowing is proportional to the amount of inversion charge present in the channel, in which, by charge neutrality of the entire device, must be equal to the amount of charge on the gate, in the absence of other charge-accumulating phenomena, such as insulator charges or work function differences. This way, the FET can be seen as a charge sensor device. The physical treatment of the FET attempts to

relate the amount of voltage applied between the gate and the substrate to the amount of inversion charge accumulated in the channel. This charge distribution in the channel can then be related to the amount of current flowing in the channel for a given source-drain bias. [32]

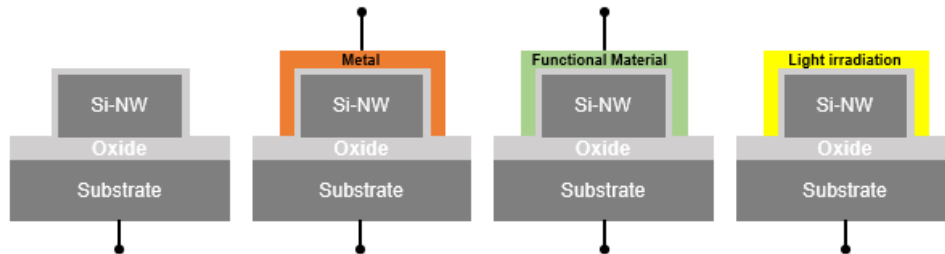


Figure 2.4. Structural evolution of functional gate field-effect transistors.

The back gate is not used to a primary gate controller. However, using a back gate has an advantage when one creates a ‘manual’ front gate to obtain complex gate controllability keeping the typical transistor behavior. **Figure 2.4** shows several variations of the back-gate FETs. The open front channel area can be combined with any material from the metal, organic, and liquid. For example, the ion sensing in the ISFET is the liquid gate combination and the double or tri-gate FET structure is one of the combined structures. Functional hybrid FETs can be created for tailored applications by combining functional materials with specific properties and additional stimuli.

2.2.2. Si-NW Bio-FET.

The first report of Si-NW bio-FET was demonstrated in 2001, for measurement of hydrogen ion (pH) concentration [33]. The p-type Si-NW device was used as a pH sensor by silanizing the silicon oxide surface with 3-aminopropyltriethoxylane, which creates amino groups along with the naturally occurring silanol (Si-OH) groups. The amino and silanol shared function as receptors for hydrogen ions, which lead protonation/deprotonation reaction, as a result of that changing the net nanowire surface charge. Then some further research shows that the Si-NW bio-FET have a lot of potential for variety of applications owing to their advantages

such as simplicity, high sensitivity, handling small amounts of target molecules, real-time capability, and rapid detection. In addition, the Si-NW bio-FET has the advantage of miniaturization and making it possible to be a portable measurement device. This detection device can be fabricated by either bottom-up or top-down, and each method has its advantages. In our experiments, top-down method was used to fabricate the sensors using silicon on insulator (SOI) wafer.

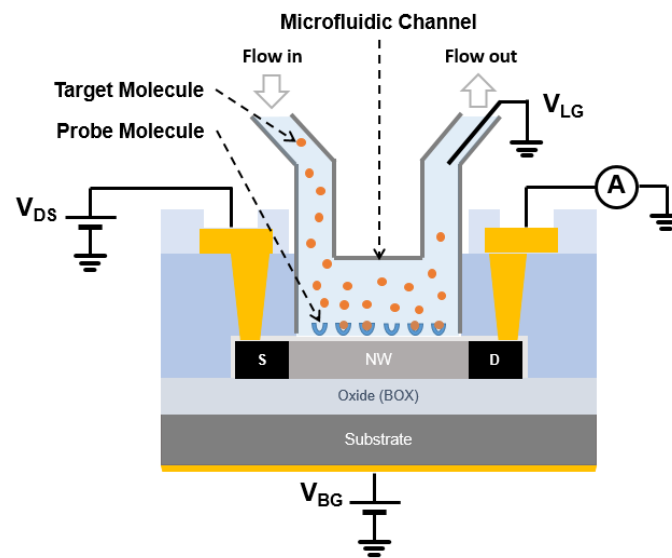


Figure 2.5. Schematic illustration of (a) a typical field-effect transistor biosensor and (b) transfer characteristics of n-type field-effect transistor for more positive charge accumulated in the surface.

Similar to the structure of MOSFET, the Si-NW FET comprises of source (S), drain (D) and gates electrode. However, the front metal gate of a Si-NW bio-FET is generally replaced by probe molecule and usually operates in the physiologically-like ionic solution environment. An additional back gate is introduced to modulate the number of conduction carriers to reach an appropriate measurement condition. The schematic illustration of a typical Si-NW bio-FET is shown in **Figure 2.5**. Upon the interaction of probe and target molecule, the electric field that field effect transistor experienced may be changed, resulting in a variation in the source-drain current. Taking n-type Si-NW bio-FET as an example, the measured current will decrease

if the probe-target interaction accumulates negatively charged biomolecules on the nanowire surface. Conversely, for p-type Si-NW bio-FET, the measured current will increase, thus the resistance will decrease.

The general expression for drain current in the saturated region in bio-FET, with assumption of n-type transistor, is

$$I_{DS} = \frac{\mu_n C_{ox} W}{L} \left[\frac{(V_{ref} - V_T)^2}{2} \right] \quad (2.1)$$

where μ_n represents the mobility of electrons in the inversion layer, C_{ox} represents the gate oxide capacitance per unit area, V_{ref} represents the applied gate or reference voltage, and W represents width and L represents length of the channel, respectively. The threshold voltage (V_T) for a bio-FET can be expressed as:

$$V_T = E_{ref} - \psi_o + \chi_{sol} + \frac{\phi_{Si}}{q} - \frac{Q_{ss} + Q_{ox} + Q_B}{C_{ox}} + 2\phi_F \quad (2.2)$$

Here, E_{ref} represents the reference electrode potential relative to vacuum. χ_{sol} represents a constant of the surface dipole potential of the solution. ψ_o represents the surface potential, which results from a chemical reaction, governed by the dissociation of oxide surface groups. χ_{sol} along with ψ_o gives the interface potential at the gate oxide–electrolyte interface, Q_B represents the depletion charge in the silicon, ϕ_F represents the Fermi-potential, ϕ_{Si} represents the silicon work function, Q_B represents the surface state density and Q_{ox} represents the fixed oxide charge. From the expression of threshold voltage, it can be observed that all terms in its expression are constant, except ψ_o , which explains the sensitivity of ISFET to the pH of electrolyte, which controls the dissociation of the surface oxide groups [34]. It is clear that the oxide–electrolyte interface, plays important role on designing a bio-FET with high sensitivity and selectivity.

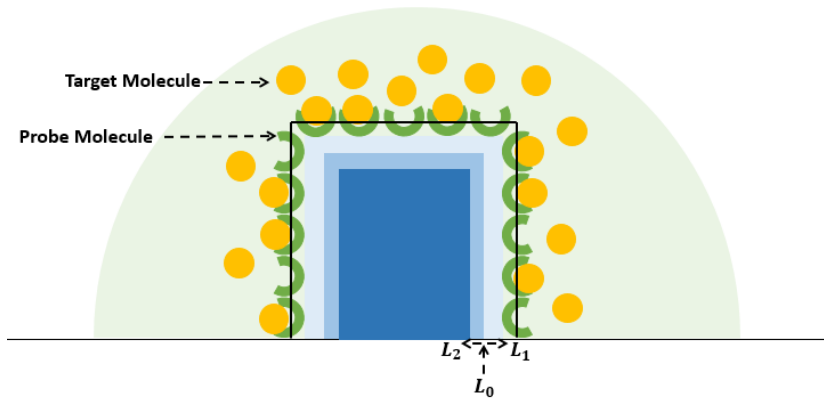


Figure 2.6. Illustration of cross-section of bio-FET during molecular interaction.

We illustrated the bio-FET from the cross-section view inside the nanowires as shown in **Figure 2.6**, where the probe molecule attached in the top of the nanowire surface. In the case of n-type nanowire where the nanowire dominated by electrons, initial carrier depletion is marked as L_0 , which is governed by the silicon oxide interface trap density and carrier concentration. During introduction of the target molecule, it creates interaction between probe and target molecule with positively or negatively charged. When generating negatively charged molecules in the nanowire surface, it leads to a decreases of charge carriers in the sensing area due to electrostatic repulsion, and the depletion region would move from L_0 to L_2 . As the effective width decreases, the source-drain current decreases. When having positively charged molecules, it leads to an increases of charge carriers in the sensing area due to electrostatic attraction, and the depletion region would move from L_0 to L_1 . As the effective width increases, the source-drain current increases. This illustration can also be extended to the behavior of p-type Si-NW.

2.2.3. Photosensitive Si-NW Bio-FET.

Recently, phototransistors have received a lot of attention for imaging and optical communication applications, which detect and convert light into electrical signals. It is critical to gain a thorough understanding of how light interacts with matter in order to easily control the photo-generated current of phototransistor. In theory, the intensity and wavelength of light can change the photocurrent level in the photosensitive device. **Figure 2.7** shows the photoelectric process for conversion of photons into an electric signal. A photon incident on a semiconductor is absorbed when it has equal or more energy than the bandgap energy of the material to break one of the lattice bonds, freeing a valence electron into the conduction band and leaving behind a hole. The photon energy is given by $E = h\nu$, where h is Planck constant and ν is a photon frequency.

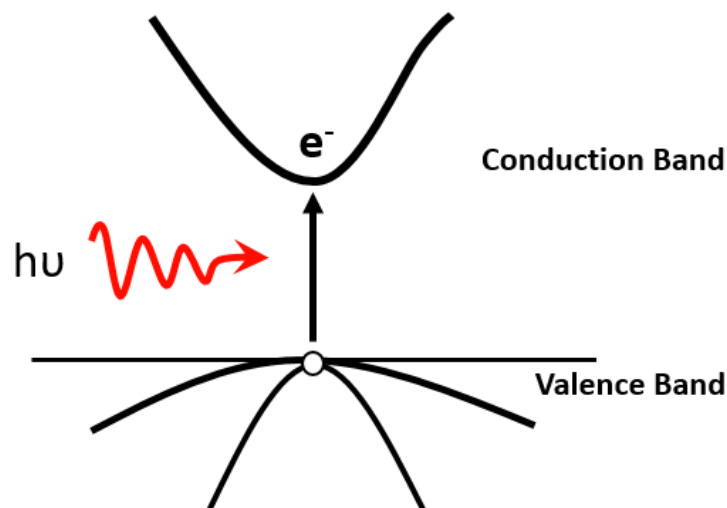


Figure 2.7. Illustration of the photoelectric process in a semiconductor material. A photon is absorbed when it has enough energy to excite an electron from the valence band to the conduction band, leaving behind a hole.

The investigation of photoconductivity in silicon has a long history due to the characteristics of silicon being suitable for electro-optical applications. By having an energy band gap of 1.1 eV, silicon is a good photoconductive material with a range of ultraviolet to visible wavelengths. Noted that silicon is an indirect band gap material; the photoconductivity

of Si-NW is associated with phonon-assisted photoexcitation. In 2005, photocurrents of single Si-NW FET developed by bottom-up synthesis fabrication technique was investigated using optical scanning measurement. the study shows that the photocurrent of the FET depends on the gate bias and the light intensity. This open a further development for nanowires as optoelectronic application. In 2016, the highly doped junctionless Si-NW phototransistor has been investigated that shows a highly sensitive photoresponse of in infrared region, which is dependent on the light power.

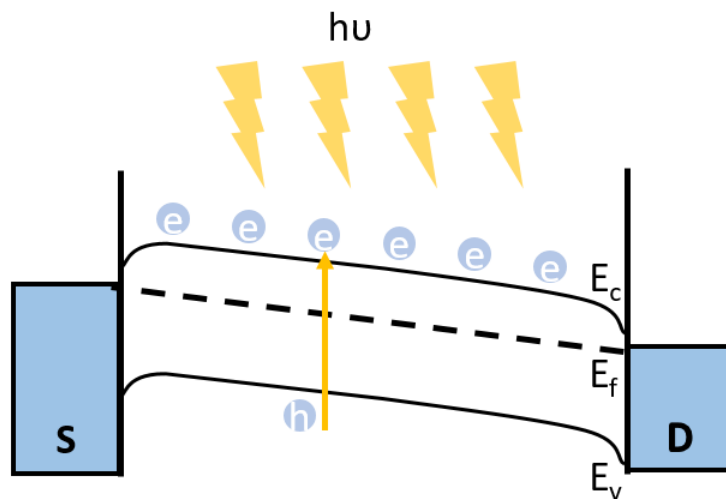


Figure 2.8. mechanism of photocurrent generation in Si-NW FET

The mechanism of photocurrent of Si-NW FET is illustrated in the **Figure 2.8**. The light illumination causes the photoexcitation of electrons which results in electron/hole pairs due to the absorption of photons with energy near or greater than the band gap energy of the silicon. Therein, any changes in the generated electron/hole pairs density lead to extra carriers that enhance the electron in the nanowire.

2.3. Debye Length Screening

In an ionic solution that has reached equilibrium, if an external charge is placed in it, the charge will cause the surrounding ions to move and the direction of the electric field to change, thus forming an electric double layer. However, substances beyond a certain distance will not feel the existence of this charge. This phenomenon is called the Debye Screening Effect

[35,36], and the range of the maximum distance that can be sensed is called the Debye length (λ_D):

$$\lambda_D = \sqrt{\epsilon k_B T / e^2 N_i} \quad (2.3)$$

where ϵ represents permittivity of a free space, k_B represents the Boltzmann constant, T represents the absolute temperature, e represents the electron charge, and $N_i = 2N_a I$ represents the ionic concentration of the solution, N_a represents the Avogadro's constant and I represents the ionic strength. In a stable solution, the addition of negatively charged particles will cause the positive ions in the solution to be attracted by the negative charge, and the negative ions will move away due to the negative and negative repulsion, until it is easy to maintain the equilibrium state. And because the direction of the electric field generated by the ion and the electric double layer is opposite, the positive and negative of the two electric fields are just offset at the radius of the Debye length in the ion distance. If the distance exceeds the Debye length, other ions cannot feel the negative force. The existence of charged particles, so the phenomenon is called Debye shadowing effect.

2.4. Surface Modification and Functionalization of Silicon Oxide

Silanization is the process of covering a surface with organofunctional alkoxy silane molecule. This process is important to form a bond between mineral material, such as glass and oxide material and organic material. The organofunctional alkoxy silane molecules have both organic and inorganic properties [37-39]. Silanization surface are usually hydrophobic, but surface properties can be adjusted by varying the side chains of the silane compound. This process has attracted extensive attentions due to the critical role of molecule assembly in the sensing electronics involving hybrid structures, especially in the hetero-interface between organic and semiconductor oxides. The silane coupling agents such as APTES, GOPTES, TPMS, MPTES, and with head-and tail functional groups are widely used interfacing

molecules, and assembly of these molecule is essential in surface functionalization technologies as shown in **Figure 2.9**.

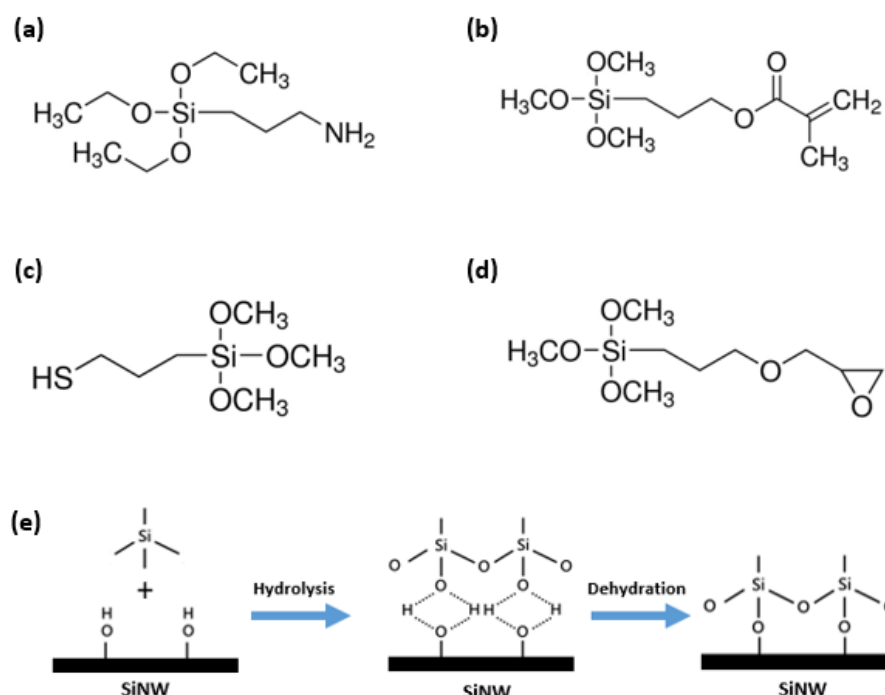


Figure 2.9. Molecular structure of (a) APTES, (b) TPMS, (c) MPTES, and (d) GOPTES. (a-d from website of Sigma-Aldrich) (e) Schematic of fabrication of silane molecules monolayer

Among of the silane coupling agents, APTES is a popular choice as it allows for further attachment of molecules through its terminal amines and also exhibit self-assembly. In this study, APTES was used as a silane coupling agent for the silicon wire on the surface of the silicon field effect transistor. We use APTES as the first layer modification method to facilitate the subsequent immobilization of probe molecules. However, in the connection of APTES, it is impossible to arrange high-density and excellent monolayer molecules. According to the chemical properties of organosilanes and intermolecular hydrogen bonds, the molecular configurations and surface structures that may be formed may have the following types, as shown in the **Figure. 2.10**. The possible structural arrangement of APTES molecules by linking the inorganic materials through the silanization reaction [40], moreover, the incorporation of

residual hydrocarbon impurities into the APTES layer cannot be ruled out. This result found that on the APTES-modified surface, only a small part of the surface was blocked by NH₂ groups, and the rest could be used for further chemical reactions.

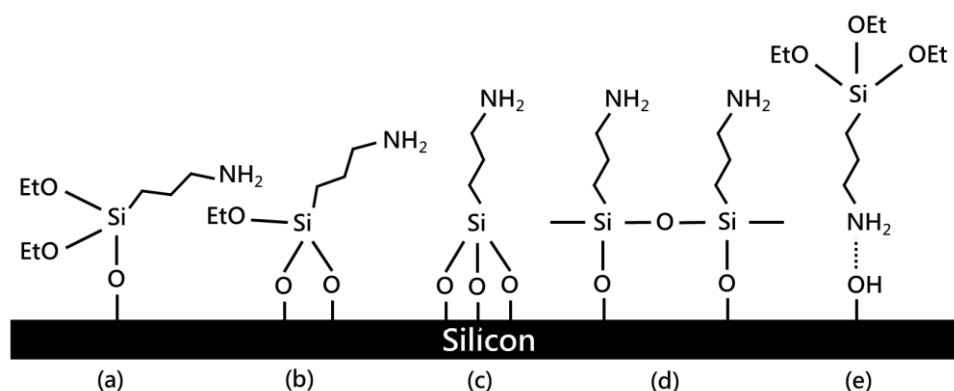


Figure 2.10. Molecular arrangement of APTES connecting inorganic materials through silanization reaction. There are five different molecular structures in the above figure, of which (a) to (d) are all covalent structures composed of surface hydroxyl groups and silanes, and (e) is the surface hydrogen bonding reaction between amine groups and hydroxyl groups

2.5. Enzyme-linked Immunosorbent Assay (ELISA) and NGAL

Enzyme-linked immunosorbent assay (ELISA) is a plate-based assay technique designed for detecting and quantifying soluble substance like peptides, proteins, antibody, and hormones. The detection is accomplished by measuring the activity of the enzyme and substrate which produces a colored solution. ELISA was first published in 1971 by Peter Perlmann and Eva Engvall of Stockholm University, Sweden, which confirmed the use of alkaline phosphatase (ALP) as a label and rabbit immunoglobulin G (IgG) as a quantitative assay for antigen [41]. At present, this technique has been commonly used as a gold standard for various clinical diagnosis [42,43].

ELISA is an immunological technology based on plate assay. It mainly uses the specificity between antibodies and antigens to detect samples. Quantitative analysis after the color reaction can quickly achieve the purpose of detection and screening. Often used to measure antibody or antigen concentrations in blood.

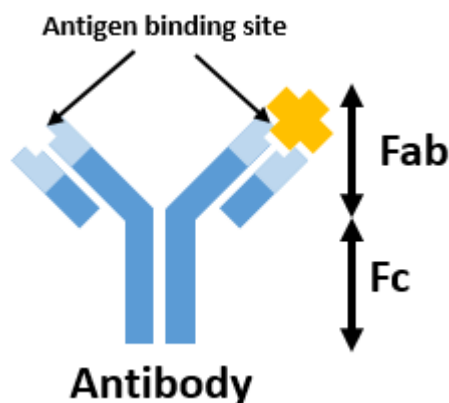


Figure 2.11. Schematic diagram of antibodies. Antibodies have antigen-binding sites that bind to antigens in their structure, are highly specific, and can recognize specific substrates.

Both antibodies and antigens use the variable regions in the antibody to identify the unique characteristics of a specific antigen. As shown in **Figure 2.11**, all antibodies have the same basic structure F-antigen-binding (Fab) region and F-crystallizable (fc) region. The Fab region consists of four polypeptides, two heavy chains and two light chains joined to form two identical arms regions. The Fc region is located in the tail and attached by a flexible hinge region to the stem of the antibody. The Fab region are antigen binding sites. It composes of a hundred amino acid sequence that give the antibody its specificity for binding antigen. In this site, antigens are bound to antibodies through weak chemical interaction and bonding is essentially non-covalent bonds such as electrostatic interaction, hydrogen bonds, Van der Waals forces, and hydrophobic interactions. The Fc region also binds to various cell receptor and protein. In biosensor, the surface modification process uses the glutaraldehyde crosslinker to immobilize the antibody in the sensing area.

ELISA detection method can be designed according to sample type and bonding method. Common ELISA methods [44] include direct ELISA, indirect ELISA, and sandwich ELISA, as shown in **Figure 2.12**. In the direct ELISA, enzyme conjugated antibody binds to antigen on the surface. In the indirect ELISA, similar to direct ELISA, but primary antibody is not conjugated and secondary conjugated antibody is used to detect the primary antibody. And

in the sandwich ELISA, the antigen is bounded by two antibodies, primary antibody and secondary conjugated antibody, specifically in between and making a complex sandwich structure. The conjugated antibody-enzyme reacts with the substrate to produce a colorimetric, chemiluminescent, or fluorescent signal. That can be detect by optical sensor.

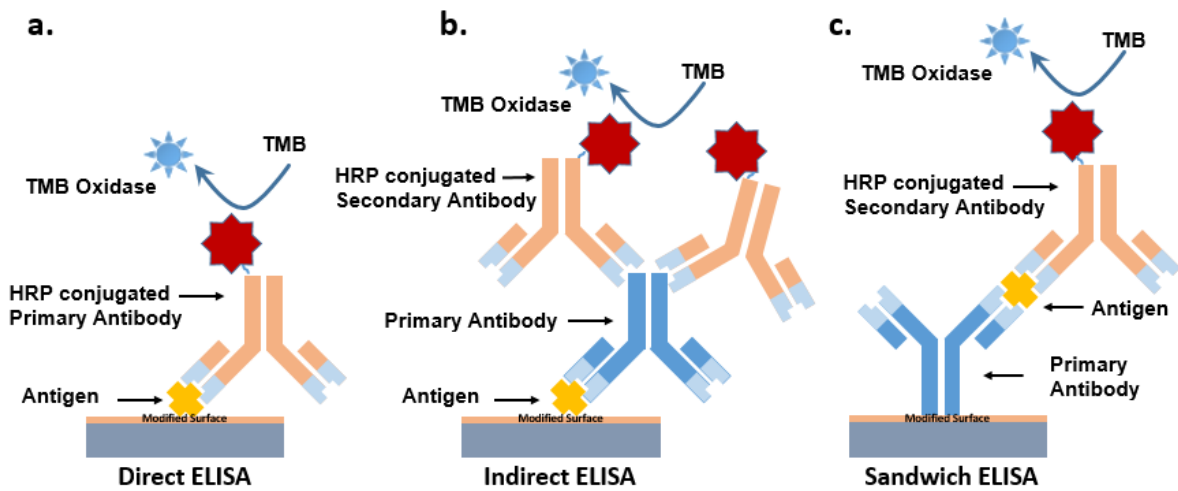


Figure 2.13. Schematic diagram of common ELISA method using HRP enzyme and TMB substrate: (a) direct ELISA method, (b) Indirect method, (c) The sandwich method. The TMB oxidase is the final step of ELISA which produce the colored solution.

Among of the produced signal in ELISA, colorimetric is the most common type in ELISA detection. Generally, there are two enzymes that conjugated to antibody, horseradish peroxidase (HRP), alkaline phosphatase (ALP), glucose oxidase (GOD), and B-Gal (B-galactosidase). That enzyme reacts with a chromogenic substrate like O-phenylenediamine (OPD), 3,3',5,5'-tetramethylbenzidine (TMB), 2,2'-azino-bis (3-ethylbenzthiazoline-6-sulfonic acid) (ABTS) solution, and etc. This method uses absorbance to determine the quantitative concentration of the antigen-antibody. The HRP and TMB is a popular and sensitive as a chromogenic enzyme and substrate pair with the relative detection sensitivity hierarchy as follows: TMB > OPD > ABTS. [45,46]

Neutrophil gelatinase-associated lipocalin (NGAL), also known as lipocalin 2 (LCN2), belongs to the apolipoprotein superfamily, is a 25 kDa protein identified as the lipocalin

superfamily. NGAL was first discovered in active neutrophils, but it has now been discovered that many other cells, including renal tubular cells, can also create it in response to various stressors. [47] For many years, NGAL has been considered a promising biomarker. It is available commercially for validation of NGAL detection in Urinary Tract Infection (UTI). NGAL is known to be upregulated within the uroepithelium and kidney of patients with UTI. Recurrent UTIs have been known to be associated with sudden kidney failure which may occur over a period of a few hours to days 18. [48] Early diagnosis and timely treatment of such UTIs are important in preventing chronic kidney injury which can be led to life-threatening illness. NGAL is usually detected by ELISA technique.



Chapter 3 Device Fabrication and Measurement Technique

In this chapter, the experimental methods will be discussed. The top-down device fabrication of bio-FET will be introduced with details. The surface modification and functionalization process will be explained step by step, including the detection procedure for molecular charge and molecular absorption. The details of the materials will be listed clearly in this chapter.

3.1. Device Fabrication of Si-NW Bio-FET

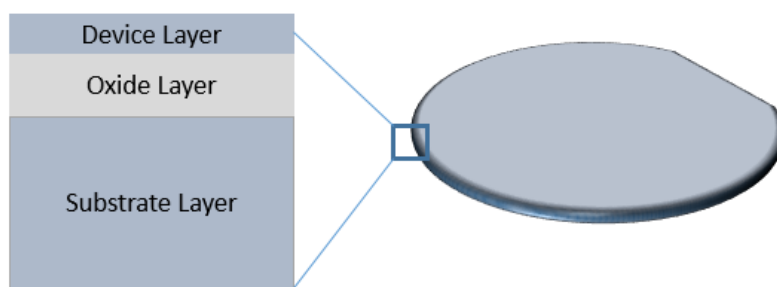


Figure 3.1. Structure of SOI wafer. The thicknesses of top Si layer, buried silicon dioxide layer are 100 nm, 375 nm and 725 μm .

Fully depleted SOI wafers have recently attracted attention in electronic application. In the semiconductor industry, the use of SOI wafers provides improved performance such as low source/drain junction capacitance, low source/drain junction leakage current, and steep subthreshold slope. Moreover, in terms of device manufacturing, the SOI wafers simplifies the fabrication process, and enables the unique device structure for future generation of integration devices. As shown in **Figure 3.1**, Our device is based on SOI wafer, which offers a multi-layer structure, consisting of top silicon layer, insulator layer, and substrate layer. The silicon layer is a thinner single crystal p-type Si $\langle 100 \rangle$ located at the top with a thickness of about 100 nm.

The insulator layer is a silicon dioxide layer with the thickness of about 375 nm. The substrate layer is a p-type silicon with the thickness of 725 μm .

Si-NW bio-FET were fabricated using top down technology on a 6 in SOI mentioned above. The top silicon layer was n-type doped with phosphorus for a concentration of $1 \times 10^{11} \text{ cm}^{-2}$ and energy of 20 keV to create accumulation-mode FET. The accumulation-mode FET significant advantages such as improve the sensitivity, low biasing power, higher current drive, and less process variability than inversion-mode FET [49-51]. Dopant activation was followed using rapid thermal annealing (RTA) in 1000 $^{\circ}\text{C}$ for 20 s to achieved the channel concentration about 10^{16} cm^{-3} . This layer was etched using standard electron beam lithography for the nanoscale wires. The nanowire was formed on top of the SiO_2 insulating layers via inductively-coupled plasma reactive-ion etching (ICP-RIE) to define the active region including the source and drain. The nanowires were subjected to form a layer of SiO_2 on the surface for two purposes; surface chemical modification, and electrical isolation with liquid solution in the biomolecule sensing setup. The thermal oxidation process is selected to decrease the density of surface dangling bonds on the Si. It was carried out at 900 $^{\circ}\text{C}$ for 20 minutes in a wet oxidation furnace to produce an oxide layer with a thickness of 15 nm. A deposition of a 150 nm polysilicon process was followed at the active area to protect the following process. Further source and drain doping was performed with arsenic for a concentration of $1 \times 10^{14} \text{ cm}^{-2}$ to reduce contact resistance of the source/drain region, followed by RTA in 1000 $^{\circ}\text{C}$ for 20 s. Interlayer dielectric (ILD) then was formed to prevent the crosstalk to adjacent metal lines. A lithography process was followed for source-drain metal contact. A metal stack of 800 nm aluminum (Al) on 150 nm titanium (Ti) was evaporated and followed by lift-off process for source/drain contact pads. The source/drain line then was passivated by silicon oxide and nitride to avoid direct contact to the sample solution. And etching process was used to remove the ILD and polysilicon on top of the Si-NW to expose the sensing area. Finally, the double gate Si-NW FET was created

and ready for the surface modification and detection. The SEM images of the Si-NW FET with channel 3 μm length, 200 nm wide, and 100 nm thickness, respectively, is shown in **Figure 3.2**.

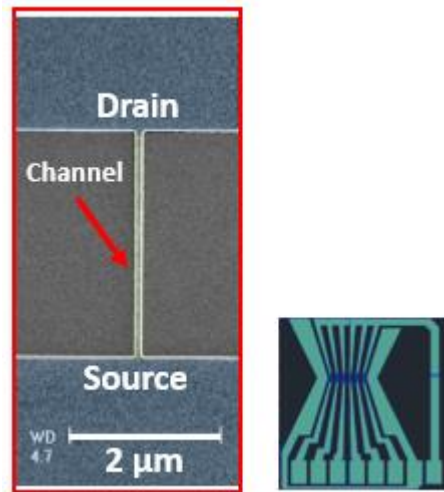


Figure 3.2. The SEM image of the FET device with channel length, width, and thickness of the wire equal to 3 μm , 200 nm, and 100 nm, respectively.

3.2. Fluidic Channel

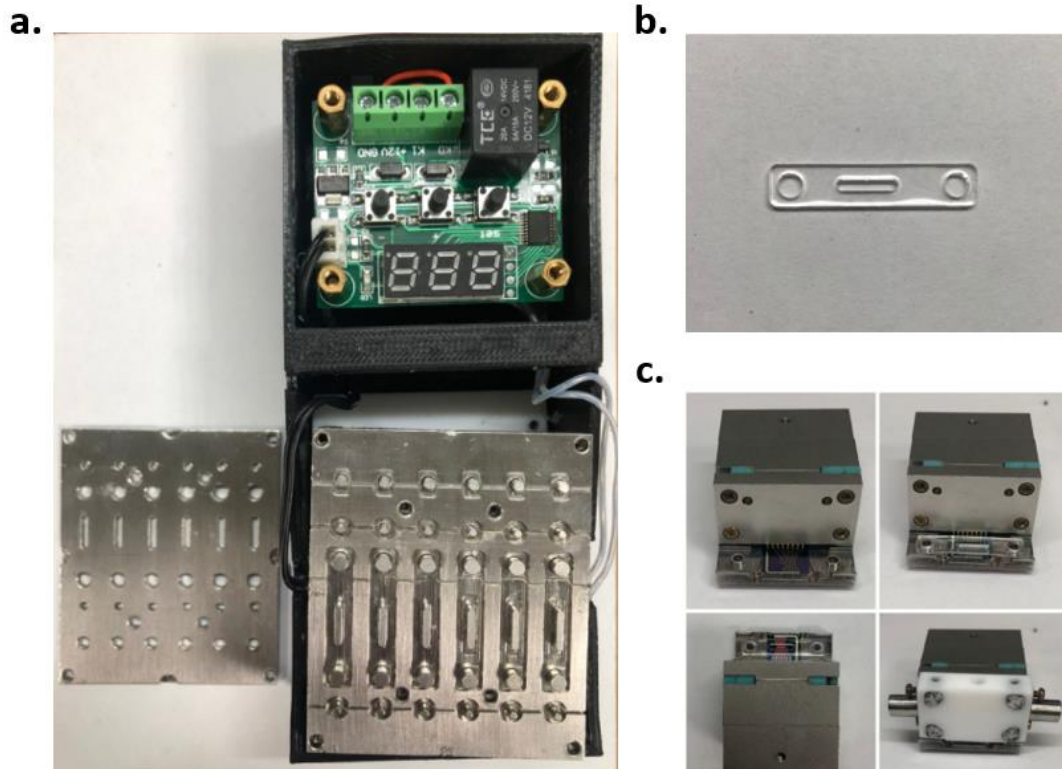


Figure 3.3. (a) fluidic channel mold, (b) fluidic channel slabs, (c) sensor assembly.

Together we also created polydimethylsiloxane (PDMS) slabs for fluid inlet/outlet on the side and fluidic channels on the bottom. PDMS is an organic polymer silicon compound with high light transmittance, high elasticity, non-toxicity and good biocompatibility. It is often used in seals or fluidic systems. For the experiment, we design and fabricate a metal mold including the lid that can be used to cast the PDMS resin as it shown in **Figure 3.3a**. The PDMS resin and the curing agent of 10:1 was added and mixed in a plate. The prepared solution was poured into the fabrication mold and degassed in the vacuum chamber. After removal of air bubble, the lid is closed and locked with the screws at four positions to remove the excess PDMS. After that, place the mold on the heating plate and bake at 80°C for 30 minutes to obtain the PDMS fluidic channel; After removing the mold from the periphery of the mold, soak it in ethanol solvent and clean it with an ultrasonic oscillator. **Figure 3.3b** shows the fluidic channel made of PDMS. These PDMS slabs were to be aligned and attached to the sensor assembly, so that the buffer solutions with/without target molecule could be introduced and guided to the sensing area of the Si-NW without any leakage, as shown in **Figure 3.3c**. The fluidic channels measured 7.34 mm in length, 1.2 mm in width, and 1.6 mm in thickness, respectively. It can accommodate the sample solution about 14.1 μL above the chip surface.

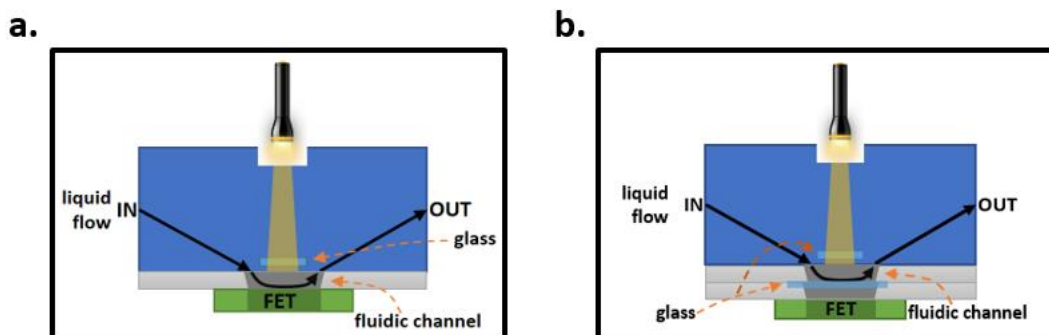


Figure 3.4. The setup of fluidic channel in sensor assembly (a) Bio-FET and (b) Opto-FET. In bio-FET, the sample solution is exposed to the surface of sensing region. And in opto-FET, the sample solution is unexposed to the surface of sensing region, FET as a photodetector.

The fluidic channel in the sensor assembly can be configured by two setups, bio-FET and Opto-FET. In the bio-FET, the sample solution is exposed to the surface of sensing region as illustrated in **Figure 3.4a**. When it exposed, the Si-NW is gated by accumulation charge in the surface due to both molecular charge and molecular absorption or light illumination. As shown in **Figure 3.4b**, for the opto-FET, the sample solution is not exposed to the surface of sensing region. The Si-NW is gated only by the light illumination.

3.3. Measurement System

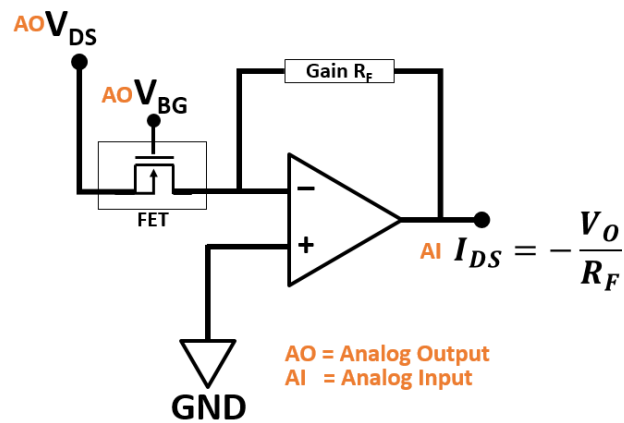


Figure 3.5. Amplifier circuit for signal amplification.

To measure the signal measured from the sensing device, we make a custom-made data acquisition system. It consists of the PCIE-6343 from National Instrument and amplifier circuit. The PCIE-6343 serves as analog output (AO) to apply DC voltage for source-drain voltage, front- and back-gate voltage and analog input (AI) to read the source-drain current. The source-drain of FET current was amplified by operational amplifiers OPA128 circuit with

the specific of gain. The output of the amplifier then connected to AI of the PCIE-6343. **Figure 3.5** displays the configuration of signal amplifier circuit for FET measurement.

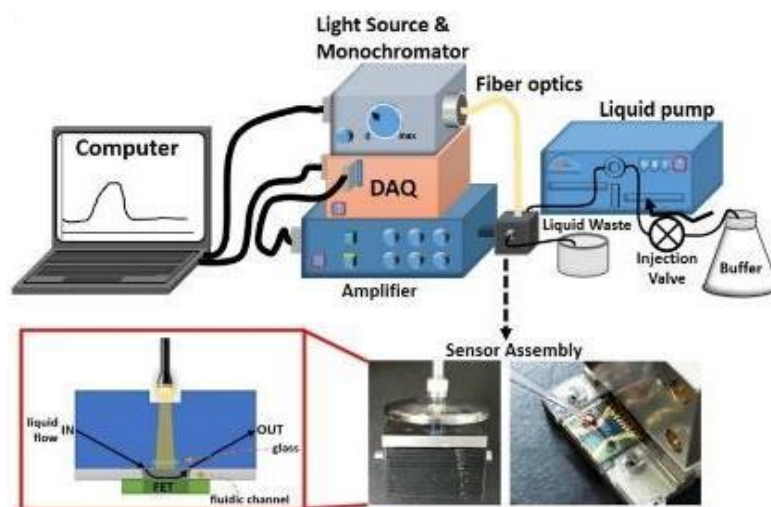


Figure 3.6. The deployment and photographs of the measurement system.

As illustrated in **Figure 3.6**, the electrical measurements of the bio-FET device were recorded by using a home-made amplifier with PCIE-6343 data acquisition (DAQ) system connected to a PC with software written with Lab-VIEW (National Instruments, USA). A bio-FET chip with an optical fiber adapter and fluidic channels are housed in the sensor assembly, linked to the custom-made data acquisition system by an HDMI cable. The fluidic channel, positioned at the two sides of the sensor assembly, was connected with the adapter for inlet and outlet solution. The inlet adapter was connected with a six-valve for sample selection and an HLPC pump (Pharmacia LKB P-500) for buffer injection. An Ag/AgCl reference electrode was inserted into outlet of fluidic channel to maintain a fixed electrolyte potential of the liquid gate. The reference electrode is set up only for the fluidic channel bio-FET configuration as shown in **Figure 3.4a**. The light source consists of a monochromator (CM110, Spectral Products) and a Xenon fiber optic light source (ASB-XE-175EX, Spectral Products) with the controlled wavelength and light intensity. The light sources were connected into the system through an optical fiber adapter and placed at the top of sensor assembly on the black dark box

at a distance of 10 mm, in order to illuminate the sensing area. In this acquisition system allows the user to control the source-drain voltage (VDS), liquid- (VLG) or/and back-gate voltage (VBG), light intensity, wavelength, and time parameter at room temperature. A commercial silicon photodiode PH-100Si (Gentech EO, Inc, USA), was used to calibrate the light intensity.

3.4. Procedure of Surface Modification and Functionalization of Silicon Oxide

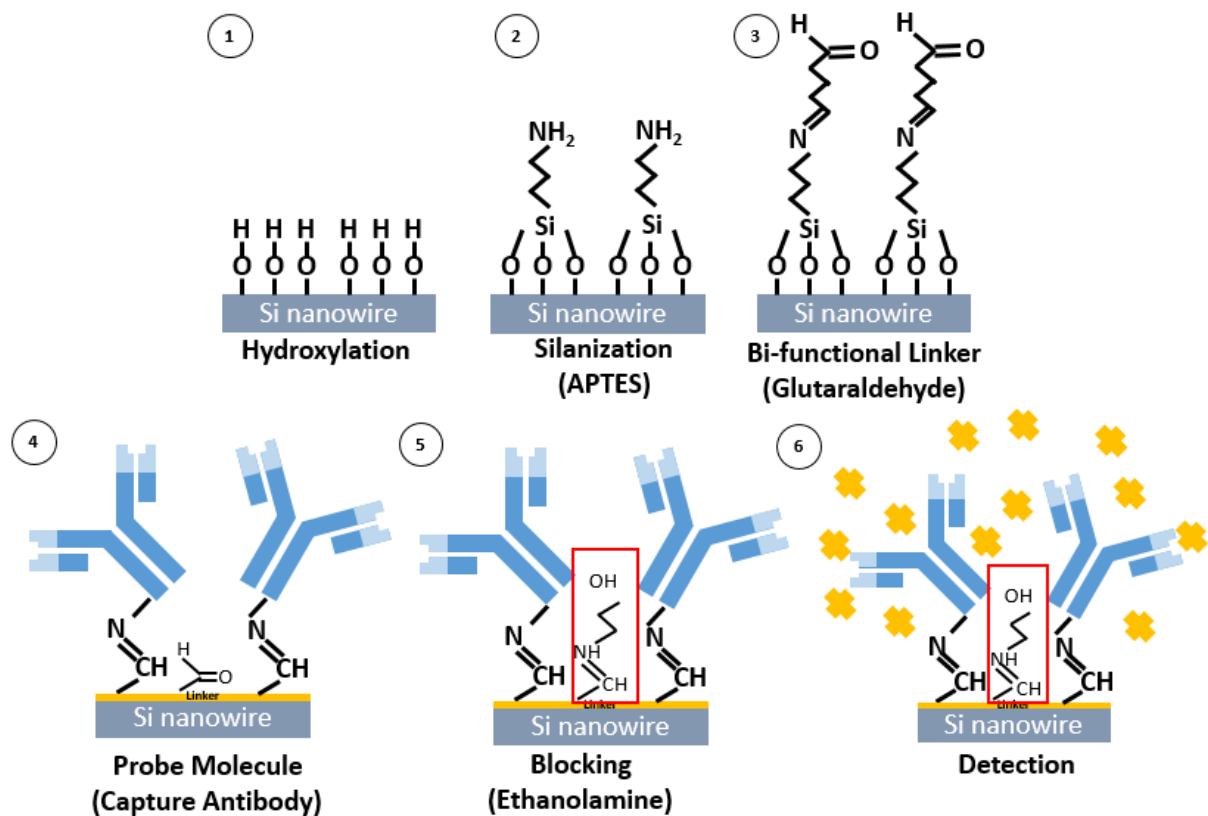


Figure 3.7. Molecule structural illustration of the probe molecules surface modification.

The cleaning process was conducted before carrying out the experiment, to ensure the cleanliness of the chip from the photoresist or a small particle in the surface. The chip was soaked in the acetone followed by ultrasonic cleaning at room temperature for 10 minutes, then rinsed it with acetone and isopropanol in sequence. We use distilled (DI) water and dry with nitrogen (N₂), bake on a hot plate at 110 °C for an hour to ensure the chip is completely dried, and ready for the surface modification process.

The primary antibody is immobilized on the surface of FET using the following procedure: First, the chip was immersed in 2% cholic acid in ethanol for 12 hours to generate -OH on the SiO₂, and purged the moisture using nitrogen. Then, the chip was soaked with APTES solution (2% in acetone) to form a single layer of APTES with amino functional group (-NH₂) on the surface, at room temperature (RT) for an hour. Then, the chip was immersed in DI water and purged with nitrogen to remove unattached molecules which then was followed by dry-baking at 110 °C for an hour. At this step, the silanization process with APTES has been completed.

Third, a bi-functional cross-linking agent, glutaraldehyde, was then used in this experiment to link the amine group of APTES and the probe molecule NGAL antibody. Glutaraldehyde have an aldehyde that can form an imine linkage with the primary amines on the protein. The chip was soaked in the 12.5% in 0.01 × PBS glutaraldehyde for an hour to form an imine bond (C=N) with APTES. Fourth, after the modification of glutaraldehyde, the NGAL antibody was immobilized onto the surface of the silicon wire which have the aldehyde group (-COH) at the end. The NGAL antibody was prepared with 1X PBS as a solvent to react with the aldehyde groups on the surface of the silicon wire for an hour. After the reaction was completed, 1X PBS was used to remove the excess probe molecules on the surface, and then the measurement can be performed. After the probe molecules are immobilized on the surface of the silicon wire, due to the large volume of the antibody itself, there may be excess aldehyde groups on the surface of the silicon wire that have not yet reacted. The sensitivity and selectivity of the FET, therefore, must be performed to block and reduce nonspecific protein adsorption. Fifth, Ethanolamine (EA) was used for blocking of the uncouple glutaraldehyde to NGAL antibody to prevent unwanted binding in further detection or experiment. The 4 mM ethanolamine was prepared with 1X PBS as a solvent.

3.5. Procedure of Molecular Charge Detection

After completing the APTES surface modification and attachment of NGAL antibody as probe molecule, the further step was the detection of NGAL antigen. The buffer solution (PBS) and bovine serum albumin (BSA) were added before the detection to confirm signal and sample selectivity. In this experiment, 0.01X PBS was used as background measurement and every sample solution was prepared in 1X PBS to prevent the molecular structure of sample from losing activity and binding affinity. Each sample measurement was followed by washing procedure to remove unbound sample, therefore the measured signal only the bounded NGAL antibody and antigen. We prepared various NGAL antigen from 0.1 pg/mL to 50 pg/mL. The real-time measurement was started after the steady current, then followed by injection of 1X PBS, 50 pg/mL BSA, and from low to high concentration of NGAL solution.

3.6. Procedure of Molecular Absorption Detection

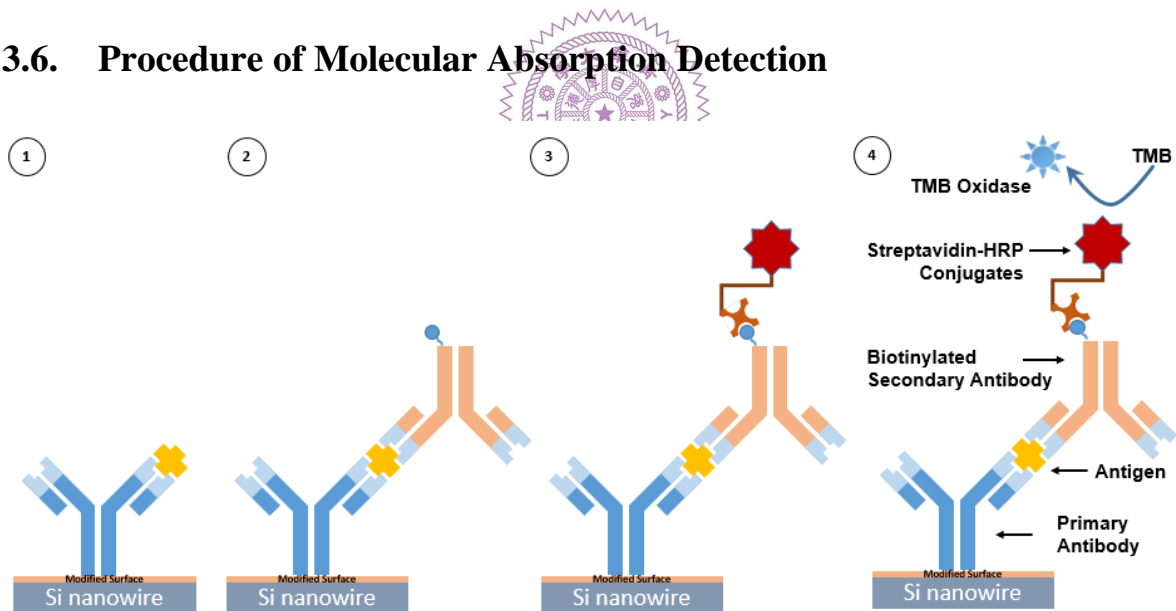


Figure 3.7. The illustration of an ELISA sandwich structure steps in Si-NW surface. Primary antibody (blue), NGAL (yellow) represents antigen, biotinylated secondary antibody (brown), conjugated HRP-streptavidin (red), and TMB (blue).

After the immobilization of the primary antibody of NGAL in the FET surface, the device is ready for the measurement. A buffer solution of 0.01X PBS was injected in to the system as background signal. As shown in **Figure 3.7**, After the NGAL antigen was bounded

into the NGAL antibody, to follow the ELISA sandwich structure in FET surface, 10 ng/mL biotinylated secondary antibody was then attached to a NGAL antibody, followed by a diluted 100 μ L conjugated HRP-streptavidin in 1X PBS with ratio of 1:40. In this process, the ELISA structure was immobilized over the Si-NW surface. The light illumination at the wavelength of interest was turned on and off alternatively. Following the introduction of 100 μ L TMB into the FET, the current versus time curves were observed for 25 minutes.



3.7. Materials

Table 3.1. List of materials for experiments

Materials	Chemical Formula	CAS number	Purity	Brand
Ethanol	CH ₃ OH	64-17-5	99.5%	Shimaku Pharmaceutical Co., Ltd.
Isopropyl Alcohol	(CH ₃) ₂ CHOH	67-93-0	70%	Tedia
Acetone	CH ₃ COCH ₃	67-64-1	-	Acros Organic
Cholic Acid	C ₂₄ H ₄₀ O ₅	81-25-4	97%	Acros Organic
3-Aminopropyl-triethoxysilane · APTES	C ₉ H ₂₃ NO ₃ Si	919-30-2	99%	Sigma-Aldrich
Glutaraldehyde · GA	C ₅ H ₈ O ₂	111-30-8	25%	Sigma-Aldrich
Phosphate Buffered Saline · PBS	-	-	10x	Fisher Bioreagents
Ethanolamine · EA	C ₂ H ₇ NO	141-43-5	99%	Acros Organic
NGAL ELISA Kit	-	-	-	R&D Systems
TMB	-	-	-	Clinical
Polydimethylsiloxane (PDMS)	(C ₂ H ₆ OSi) _n	63148-62-9	-	Boss Yuan
Ninhydrin	C ₉ H ₆ O ₄	485-47-2	0.1%	TCL
Nitrogen	N ₂	-	-	

Chapter 4 Results and Discussion

4.1. Absorption Spectra of HRP Redox Reaction with TMB

The detection signal in the ELISA methods, represents the molecular absorption due to the reaction of enzymatic activity. HRP and TMB is one of the most popular enzyme and substrate reactions. HRP conjugates with streptavidin that can specifically recognize the targets labeled with biotin and antibody. Thus the quantities of the targets are proportional to the quantity of the HRP. The HRP redox reaction driven TMB color development. TMB yields a blue color reaction product, the absorbance spectra of which are obtained from a standard spectrometer (JASCO V670). **Figure 4.1** displays the absorbance peak of the TMB reaction before and after the oxidation process. The absorbance peaks of blue products are about 372, 650, and 910 nm. At these wavelengths, the absorption increased during the TMB oxidation process. This suggests the detection at those peaks.

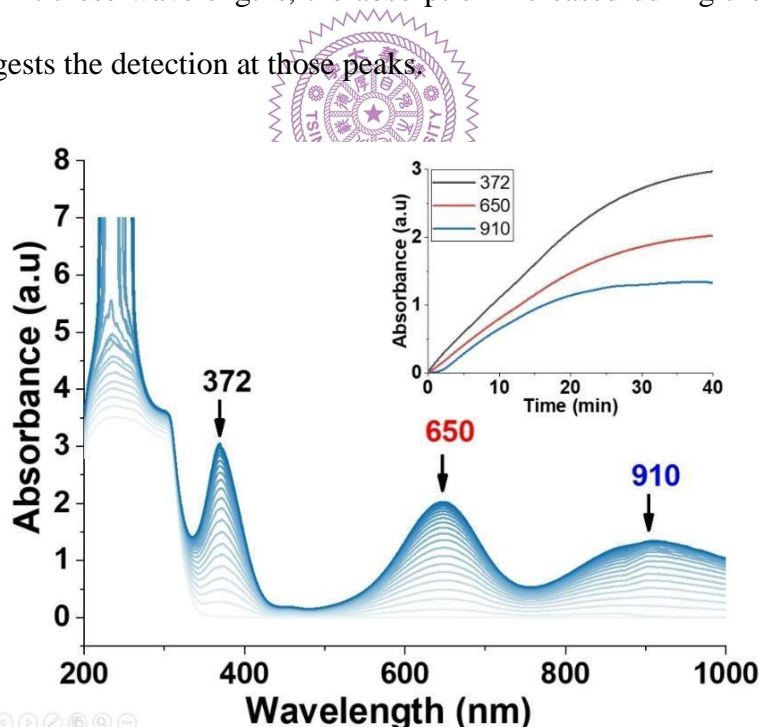


Figure 4.1. The UV-Vis absorption spectra of TMB oxidation products. Experiments were carried out using 100 μL TMB and 20 μL HRP in the phosphate buffered saline solution at pH at 7.4 and temperature at 25 $^{\circ}\text{C}$. The spectrophotometer was swept from 200 to 1000 nm and there were 20 times measurement with interval of 2 minutes. (inset) Absorption evolution of TMB oxidation product at wavelength of 372 (orange), 650 (blue), and 910 (grey) nm.

4.2. Device Characteristics of Si-NW Bio-FET

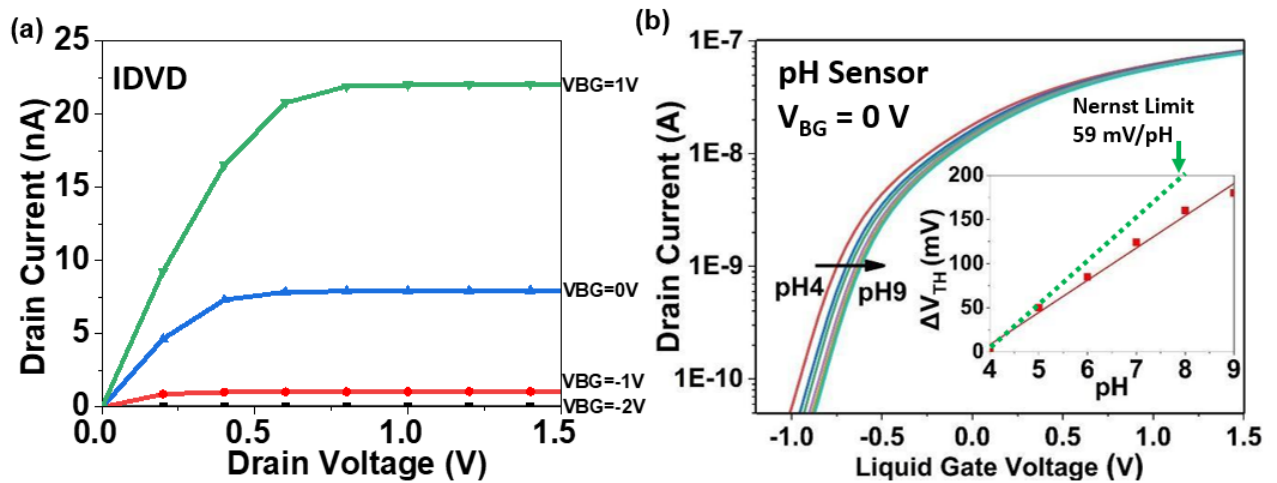


Figure 4.2. Basic characterization of FET: (a) Output characteristics of the silicon FET sensor and (b) pH sensitivity response of the FET device ranging from pH 4 to pH 9. The bias condition V_{DS} 0.5 V, V_{LG} -1 V to 1.5 V, and V_{BG} was kept constant at 0 V.

The performance of the device was first evaluated by measuring the output characteristics, IDVD. As displayed in **Figure 4.2a**, under varying VBG, the drain current increased upon increasing VBG. Even, the device draw the drain current about 7 nA at VBG 0 V, it indicates that the device is in accumulation modes as it designed. The performance of the fabricated devices was then evaluated by using pH solution to assess the quality of the surface of sensing area. We were measured output characteristics, IDVLG, and injected the different pH ranging from 4 – 9. **Figure 4.2b** displays the result of the pH sensor. The V_{TH} is defined as the liquid gate voltage at drain current of 1 nA. The results showed that the response of the device with SiO_2 gate oxide to pH was indeed highly linear with a linear fit r-square value of 0.98823. The slope of the fitting line represents the sensitivity to pH with the value of 45 mV/pH. The sensitivity of pH in this device is lower than the Nernst limit (59 mV/pH). This difference might be due to the high electrolyte screening, the oxide quality, finite semiconductor capacitance, and protonation affinity of the sensor surface.

4.3. Photosensitive Si-NW Bio-FET

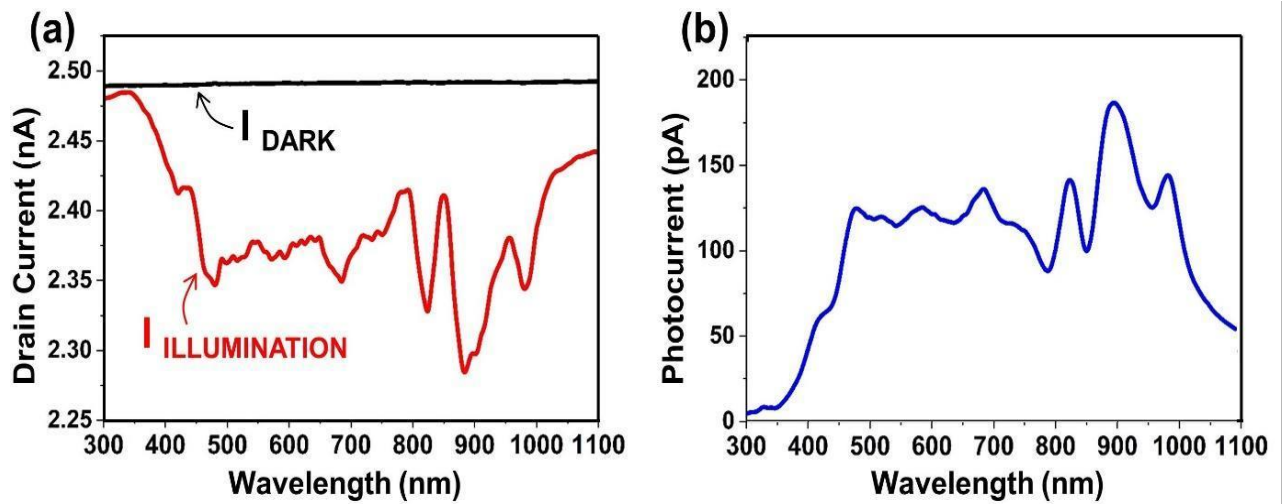


Figure 4.3. The photoresponse of the bio-FET in air. In (a), illumination current (red) and dark current (black) of wavelengths from 300 to 1100 nm. (b) The photocurrent, is expressed as the absolute value of subtraction the illumination current from dark current. The spectrum is taken with drain voltage (VDS) set at 0.5 V and back-gate voltage (VBG) set at 0 V.

We examined the photoresponse of FETs under a light source with a wavelength range from 300 nm to 1100 nm and compared it to dark current in order to evaluate the performance of FET under the light illumination. As displayed in **Figure 4.3a**, the drain current decreases upon illumination at all point of wavelength. The increasing or decreasing drain current is determined by factors such as possibly channel design, doping type and concentration, and photon wavelength [52]. We expressed photocurrent (I_{PH}) as the absolute value of change in the drain current from dark and illumination, since the magnitude of the photocurrent matters more when utilized as a photodetector than its polarity. i.e., $I_{PH} \equiv |I_{light} - I_{dark}|$. The photocurrent spectrum recommends that our FET has a suitable photoresponse in a wide-ranging wavelength between 400 nm and 1000 nm as indicated in **Figure 4.3b**.

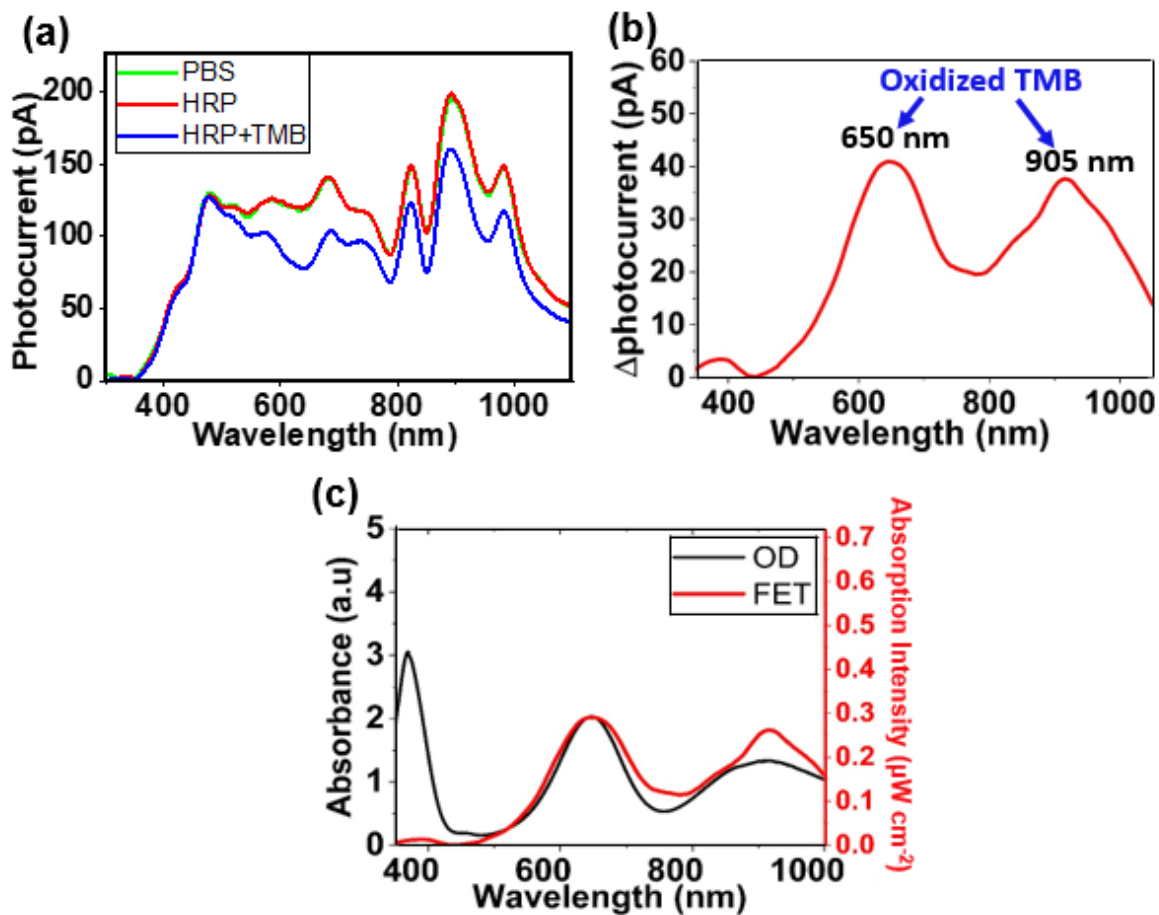


Figure 4.4. Photo-absorption spectrum of the oxidized TMB measured using a measurement setups shown in figure 3.5a (a) The photoresponse of FET in 1x PBS (green), and with HRP-surface modification (red), and after adding in TMB to react with the surface HRP (blue). (b) The result of a subtraction of “HRP” from “HRP+TMB” curve in (a). (c) A comparison between the oxidized TMB photo absorption spectrums measured using a FET (red) and a commercial spectrophotometer (black).

The Photocurrent measurements were conducted in which the bio-FET was subjected to surface modification to enable the interaction between HRP and TMB to produce oxidized TMB. The photocurrent spectrum is shown for the bio-FET under various conditions such as 1X PBS, HRP, and HRP with TMB in **Figure 4.4a**. The photocurrent spectrum measured in 1X PBS and HRP were shown to be similar. This indicates that there were no changes in the absorption at the wide wavelength range between 300 nm and 1100 nm. Following the addition of TMB, the initially translucent PBS solution gradually turned dark blue due to the presence of oxidized TMB; the photocurrent curve “HRP + TMB” was recorded after the oxidized TMB saturate. Bio-FET photocurrent decreases due to the photo-absorption by oxidized TMB.

Figure 4.4b shows the subtraction of spectra “HRP + TMB” and HRP where the oxidized TMB shows a clear absorption at the wavelengths of 650 nm and 905 nm with the peaks of 41 pA and 39 pA, respectively. Using a commercial spectrophotometer (OD), we evaluated the absorption spectrum of oxidized TMB. As displayed in **Figure 4.4c**, three peaks in the OD spectra was discernible at wavelengths of 370 nm, 650 nm, and 905 nm. By comparing that OD and bio-FET response, an extinct peak at wavelength of 370 nm is associated with the inability or insensitivity of the bio-FET to respond the light under wavelength of 400 nm.

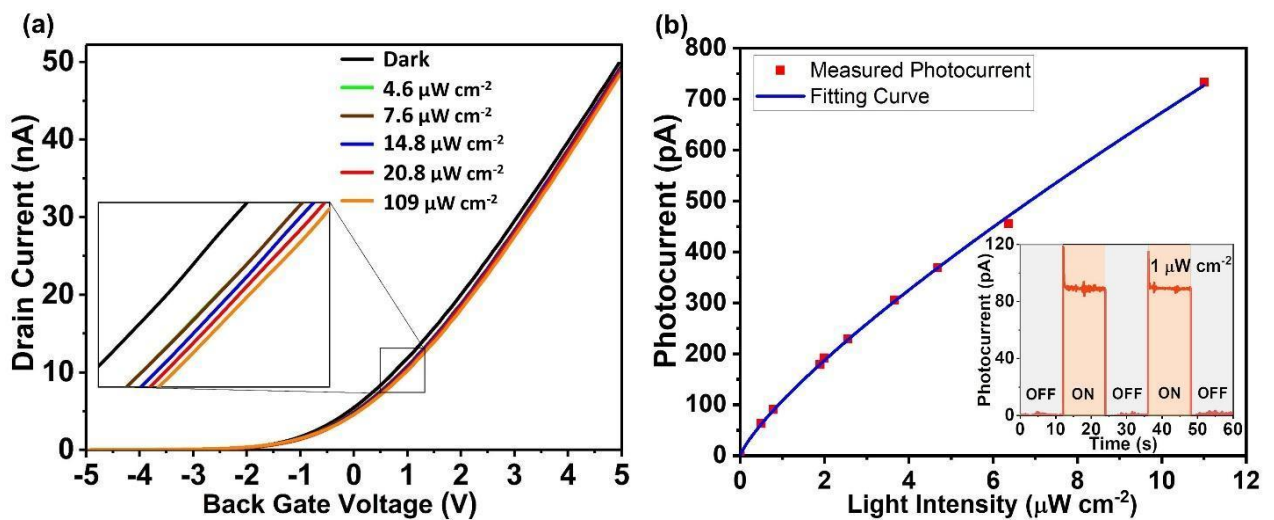


Figure 4.5. In (a) I_{DS} - V_{BG} response of the FET under various levels of light illumination: dark (black), 4.6 (green), 7.6 (brown), 14.8 (blue), 20.8 (red) and 109 (orange) $\mu\text{W}/\text{cm}^2$ with bias condition V_{DS} 0.5 V, V_{BG} -5 V to 5 V, and V_{LG} was kept constant at 0V. The current at all back-gate voltage decreases with increasing light intensity. In (b) red dots are measured photocurrent, and the black curve is the power-law fitting. The inset shows on/off photocurrent under 1 $\mu\text{W}/\text{cm}^2$ light intensity. Photocurrent increases sub linearly and follows power-law dependence for light intensity below 11 $\mu\text{W}/\text{cm}^2$

The photocurrent characteristics measured with bias condition V_{DS} at 0.5 V, V_{BG} from -5 V to 5 V, V_{LG} was kept constant at 0 V and fixed wavelength 650 nm for varying light intensity is shown in **Figure 4.5a**. The current at all back-gate voltage decreases with increasing light intensity. The absolute photocurrent is then plotted under different light intensity at V_{DS} 0.5 V and V_{BG} 0 V as displayed in **Figure 4.5b**. Enhancement in light intensity leads to an increase in device photocurrent. However, the photocurrent increases sub

linearly with excitation power. The experimental data was fitted using a power-law dependent where light intensity A is in $\mu\text{W}/\text{cm}^2$.

$$I_{\text{ph}}(\mu\text{A}) = 6.34 A^{0.794} \quad (4.1)$$

4.4. Si-NW Bio-FET Surface Modification

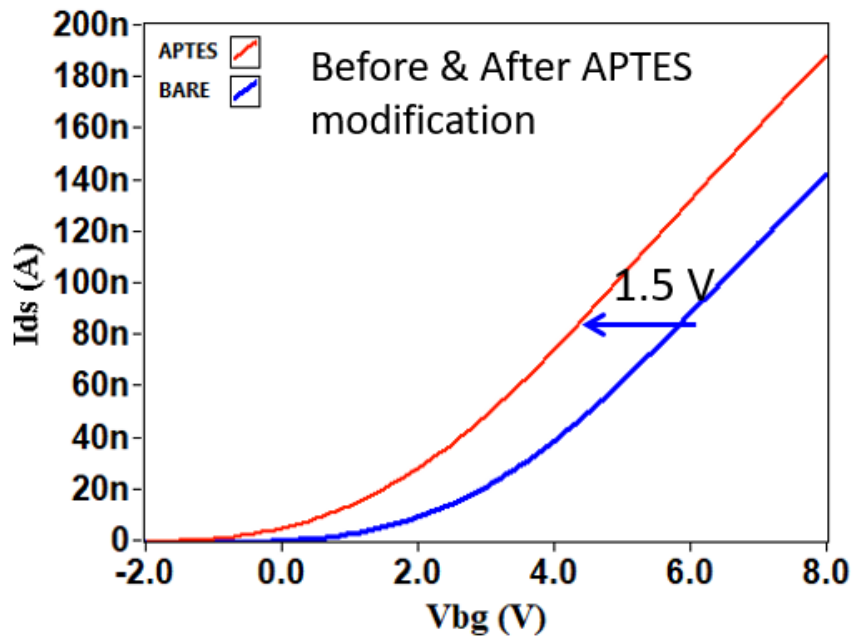


Figure 4.6. $I_{\text{DS}}-V_{\text{BG}}$ curve bare chip (blue) and after APTES modification (red) in air. the blue arrow indicate that the curve shift left after surface modification.

N-type Si-NW bio-FET is used for the detection device in this experiment. Each molecule has electrical charge, positive, negative, or equal. The molecules charge accumulated on the surface of the nanowire will affect the conductivity of the device. The cleaned bare chip was carried out by surface modification through hydroxylation and silanization process with APTES. To confirm the surface modification process electrically, we measure $I_{\text{DS}}-V_{\text{BG}}$, in bare chip and after silanization process. As shown in **Figure 4.6**, the V_{BG} shift left and current increases after the surface modification with APTES in air measurement. Due to the high electron distribution on the surface layer on APTES, the surface layer of the nanowire feels a relatively positive electric charge, so the $I_{\text{DS}}-V_{\text{BG}}$ curve shifted to the left and current increase

because the positive charge attracts more electron inside the nanowire channel. It confirms that the APTES surface modification successfully applied in the sensing area of Si-NW.

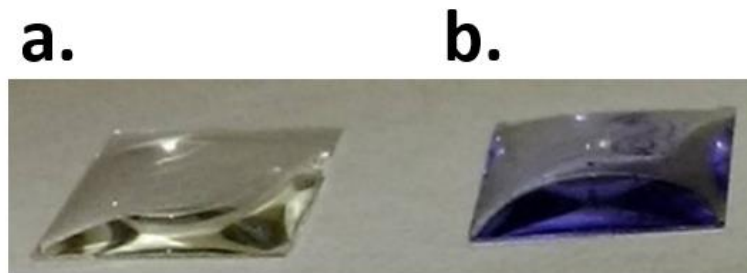


Figure 4.7. Test the Ninhydrin solution using silicon chip. (a) blank silicon chip and (b) APTES modified silicon chip. A ninhydrin solution is dropped into both chip blank and APTES modified silicon chip and the heated on 100 °C. The APTES modified chip showing blue-purple color, which indicated that ninhydrin would undergo chelation reaction with primary amine.

The APTES surface modification was also confirmed chemically. Ninhydrin was used to chelate with the primary amine at the end of APTES. First, a 1x1 cm chip with silicon oxide on top was modified according to the surface modification steps of Si-NW bio-FET. The modification was followed by rinsed and dried on a heating plate. An unmodified same size silicon oxide chip was placed side by side with the modified chip. A ninhydrin was added on the surface of both unmodified and modified chip in the same time, and then heated and reacted for about a minute. We can see that the liquid on the silicon oxide wafer in **Figure 4.7a** is colorless and **Figure 4.7b** is blue-purple color. This confirm that the APTES surface modification was successfully applied in the chip.

After the APTES surface modification accomplished, the subsequent modification steps are all carried out in the fluidic channel. Then, the modification of glutaraldehyde was carried out, and after the modification was completed, the electrical signal was analyzed. Through the displacement performance of the $I_{DS}-V_{BG}$ curve, it was judged whether the modification of each layer of molecules was successful or not, and all the modification results were drawn as **Figure 4.8**.

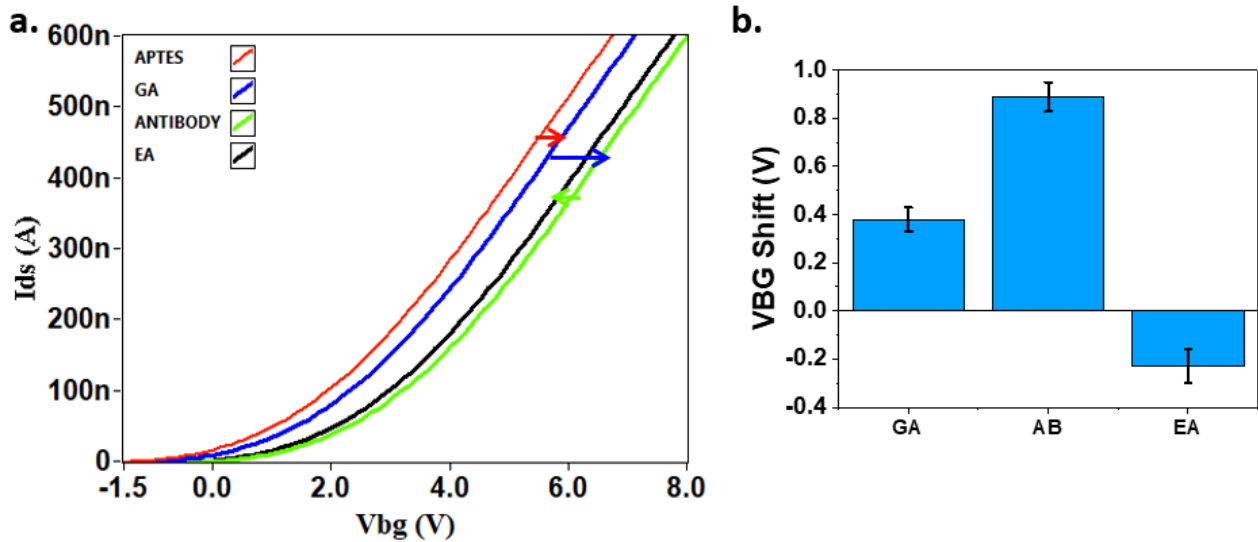


Figure 4.8. (a) I_{DS} - V_{BG} of modified molecules in buffer solution. After APTES modification (red), after glutaraldehyde (green), after ethanolamine blocking (cyan) and after Antibody (orange). (b) the V_{BG} shift of each surface functionalization.

After washing the glutaraldehyde-modified silicon field effect transistor with phosphate buffered solution (PBS) for several times, the electrical signal was measured, and the result showed that V_{BG} shifted to the right. Mainly because of the electron pushing group (-CHO) of glutaraldehyde, the surface of the silicon wire senses the electric field of negative charge; therefore, the I_{DS} - V_{BG} curve of the n-type FET electrical measurement is shifted to the right. The V_{BG} signal was observed shift about +0.38 V. Then, after the modification of the NGAL antibody, it can be clearly observed that the I_{DS} - V_{BG} curve shifts to the right. Proteins with large structures have low electron distribution, which makes the surface of the silicon wire sense a negatively charged electric field; therefore, the I_{DS} - V_{BG} curve in the electrical measurement of n-type FET will shift to the right. The V_{BG} signal was observed shift about +0.89 V. Finally, after further modification with ethanolamine, a leftward shift of the I_{DS} - V_{BG} curve can be clearly observed. This is because after the bonding reaction is completed, the aldehyde group at the end of glutaraldehyde is changed to the hydroxyl group (-OH) of the electron-withdrawing group, so that the surface layer of the silicon wire senses the electric field

of positive charge. Therefore, the I_{DS} - V_{BG} curve of the n-type FET electrical measurement will be shifted to the left. The V_{BG} signal was observed shift about -0.23 V. **Figure 4.8b** summarize the surface functionalization of each molecule in the surface.

4.5. Detection of Molecular Charge

Bio-FET was used as a charge sensor to detect changes in molecular charge caused by binding between NGAL and primary antibody. The primary antibody, which was used as a receptor, contributes to the quantification of NGAL. For that, the primary antibody was immobilized onto the FET sensing surface as described in the experimental section. The performance of the bio-FET as a charge sensor was demonstrated using different concentrations ranging from 0.1 to 50 pg/mL. The real-time measurement of various NGAL concentration is conducted under dark condition, means no light interference, as shown in

Figure 4.9. The normalized change current is defined as:


$$\text{Drain Current (\%)} = \frac{\Delta I}{I_0} \quad (4.2)$$

Where ΔI represents the change of the drain current and I_0 represents the initial values of the drain current. The drain current (%) is increased proportionally as the NGAL concentration increased in the above range.

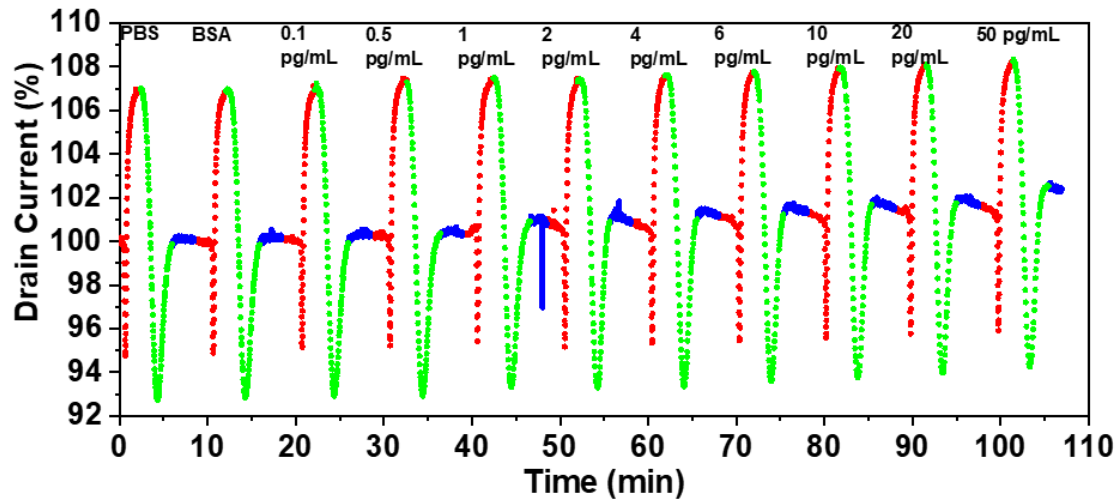


Figure 4.9. The real-time of bio-FET response to different concentrations of NGAL ranging from 0.1 to 50 pg/mL.

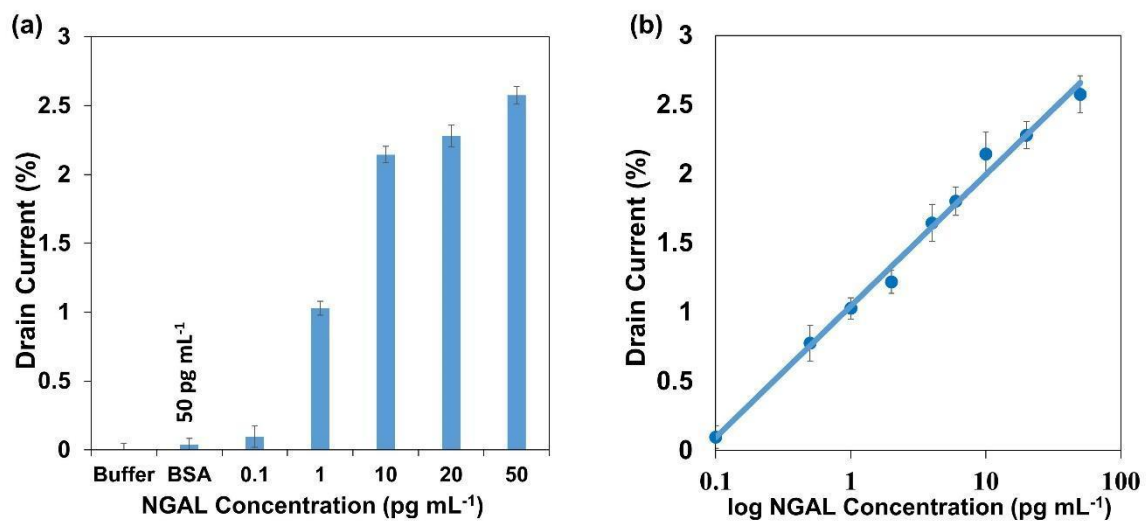


Figure 4.10. The measurement of drain current of bio-FET for several NGAL concentrations (a) ranging from 0.1 to 50 pg/mL with a high concentration of BSA as a control experiment for selectivity test and (b) drain current (%) as the function of log NGAL concentration.

Next, a low-concentration NGAL solution (0.1 pg/mL) was introduced. Since it is known that the antigen will react with the antibody on the surface of the silicon wire, there should be a current change due to the binding. The test results show that the current value increased. There is an obvious upward trend. It can be seen that when the n-type silicon field effect transistor is detected, it shows that the protein is positively charged in the environment of pH 7.4, and the electric dipole moment of the surface molecule tends to be positive after

binding. In addition, after the qualitative results are known, the analysis of NGAL at different concentrations is carried out using the same detection method for NGAL concentration of 0.5, 1, 2, 4, 6, 10, 20 and 50 pg/mL, the results are shown in **Figure 4.10a**. Since those traces have the same current height because there were no NGAL bindings and there were sets as reference currents to 100%. With increased NGAL concentration, the current in percentage increases. In **Figure 4.11**, we show the $I_{V_{BG}}$ characteristics taken in the beginning and the end of the I-time measurement.

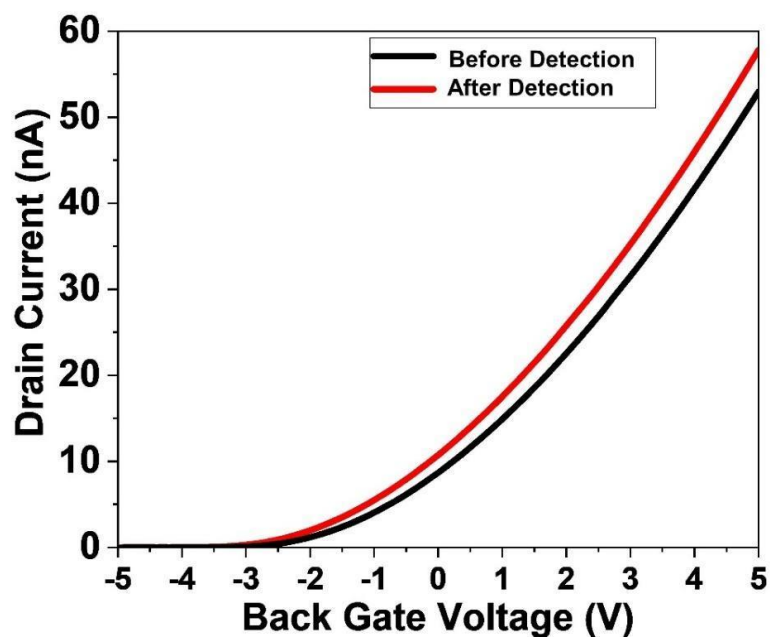


Figure 4.11. The bio-FET current as a function of the back gate voltage taken before (black) and after (red) the measurement shown in Figure 4.9.

These findings indicated that this bio-FET is a promising device for detecting specific targets molecule. Furthermore, we achieved a sensitivity of 0.1 pg/mL, which is well beyond the clinically useful level of NGAL in human serum of 40-160 ng/mL [53]. In other words, this bio-FET sensor may be potentially applicable for other very lower range biomarkers in certain diseases, such as interleukin-6 (IL-6) for respiratory failure and fetuin A (HFA) for atherosclerosis inflammatory disease [54,55]. We provide an overview of the many immunosensor methods that have been reported for the detection of NGAL, and our finding

demonstrate that the proposed bio-FET as a charge sensor possesses great bioanalytical performance among all methods, with the highest sensitivity of 0.1 pg/mL (Table 4.1).

Table 4.1. Comparison of our work with other method on NGAL detection

Sensor	Method	Range of Detection	Ref
Gold nanoparticles	CV	50-250 ng/mL	[56]
Graphene Nano Platelets	ELISA	0.5-5120 pg/mL	[57]
Carbon nanotube	ELISA	0.5-5120 pg/mL	[58]
Graphene/Polyaniline	CV	50-250 ng/mL	[59]
Silicon	FET	0.1-50 pg/mL	Our work

4.6. Detection of Molecular Absorption

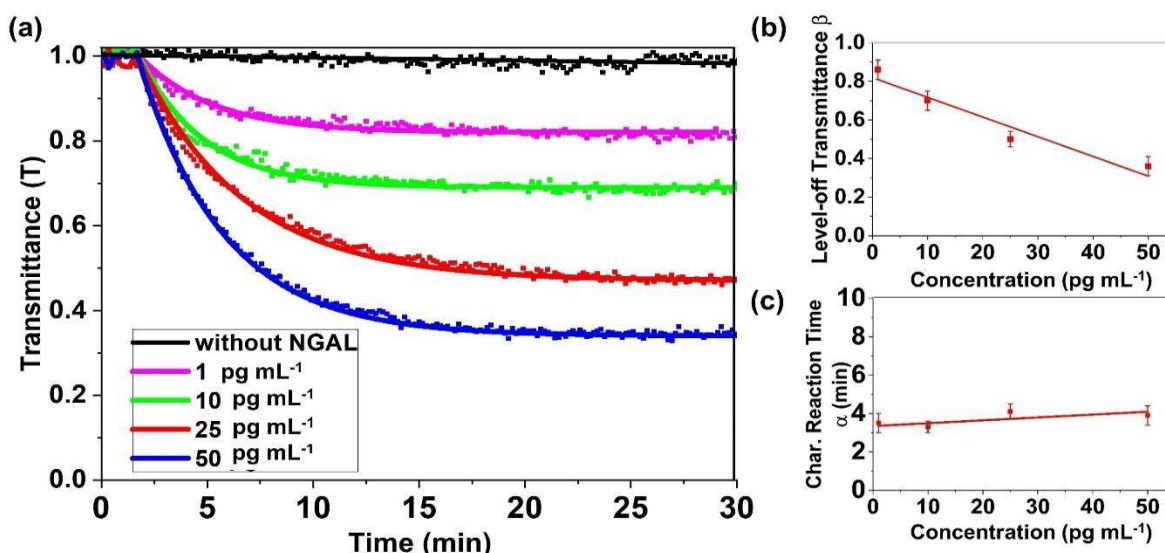


Figure 4.12. Real-time measurement of increasing oxidized TMB concentration in response to various NGAL concentrations. Transmittance traces correspond to NGAL concentrations without NGAL as control (black), 1 pg/mL (purple), 10 pg/mL (green), 25 pg/mL (red), and 50 pg/mL (blue). The experimental data are presented as colored dots, and the fittings are shown as thick solid curves with the corresponding colors. From saturation transmittance and reaction time extracted from exponential fitting $T(\text{min}) = (100 - \beta) \exp(-t/\alpha) + \beta$, one can figure out the level-off value (β) and the characteristic reaction time (α). These are presented in (b) and (c), respectively.

As described in the chapter 3, detection procedure of molecular absorption, The NGAL antigen was then conjugated to a biotinylated secondary antibody, which was then followed by a conjugated HRP-streptavidin. The ability to measure in real-time is a powerful feature of our bio-FET chip. The bio-FET was ready for photo-absorption measurement in this configuration.

Following the addition of the TMB molecule, an oxidized TMB product is produced during the reaction with the HRP enzyme.

The 650 nm light source was set to a low intensity of 1 $\mu\text{W}/\text{cm}^2$ to avoid any unwanted influence on the interaction between TMB and conjugated HRP-streptavidin. In less than 25 minutes, photocurrent measurements were conducted in the system over several on/off cycles. The presence of oxidized TMB gradually turned the originally transparent PBS solution dark blue. **Figure 4.12a** depicts the resulting photon absorption curve, which shows the decrease in solution transparency caused by the emergence of oxidized TMB. This signifies the existence of immobilized NGAL on the bio-FET surface. NGAL concentrations of 1 pg/mL, 10 pg/mL, 25 pg/mL, and 50 pg/mL were examined for quantitative evaluation. Following that, equation 4.1 was used to convert the photocurrent into the corresponding intensity. The corresponding transmittance curves for different NGAL concentrations are shown in **Figure 4.12a**. Before the introduction of TMB at 2 min, transmittance is at a maximum due to the high transparency of the PBS solution. The transmittance response caused by optical absorption reduces after the addition of TMB. An exponentially decaying function can be used to describe this tendency. We give a transmittance response in order to compare each concentration. In this instance, the intensity reading taken right before the addition of TMB (when the PBS solution is transparent) was set to unity. It was discovered that the intensity ratio decreased more rapidly the higher the NGAL concentration. This relationship, however, leveled off at 25 min. Time dependence of the intensity ratio $\gamma(t)$ can be described by the following formula:

$$\gamma(t) = (100 - \beta)e^{\frac{-t}{\alpha}} + \beta \quad (4.3)$$

where β is the leveling off value at t at 25 min. TMB reaction time α is defined as the time that intensity drops to 37% of the full range (100 - β). Leveling-off transmittance β decreases linearly with NGAL concentration as displayed in **Figure 4.12b** and characteristic time α is

independent of NGAL concentration at about 3.8 min as displayed in **Figure 4.12c**, suggesting that the rate of converting TMB into oxidized TMB is a characteristic behavior of this process. Saturation value β has a nearly linear relationship with concentration, making it possible for quantitative determination of NGAL concentration. **Figure 4.13** shows the color evolution of oxidized TMB for 50 pg/mL NGAL. It shows gradually change of the color from transparent to dark blue, indicating the increasing concentration of oxidized TMB.

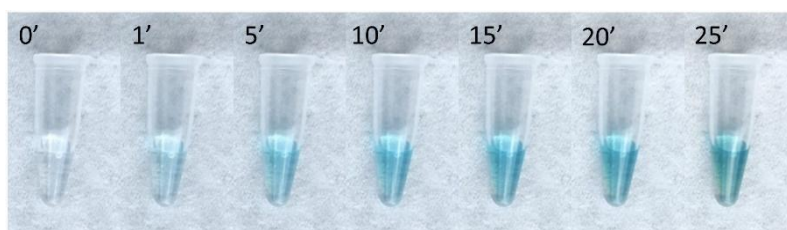


Figure 4.13. The color evolution of oxidized TMB for 50 pg/mL NGAL at different time in minutes.

4.7. Detection of Quercetin - Cu^{2+} complexes using bio-FET as photodetector

Many trace metal ions, such as Co^{2+} , Ni^{2+} , Zn^{2+} , Fe^{2+} , and Cu^{2+} , are necessary for human body and play an important role in human health [60]. The complex stability of the quercetin and copper ions is said to be the highest among these ions [61], and metal chelation in the quercetin-copper ions has been the subject of extensive research in recent years [62-66]. These studies were carried out utilizing optical spectroscopy such as ultraviolet visible (UV-Vis) spectrophotometry [67,68], infrared spectroscopy [69,70], and electrospray ionization mass spectroscopy [61]. The idea of optical spectroscopy is that the quercetin-copper complex absorption varies in the different wavelengths, depending on its complex electronic structures. Therefore, the spectroscopic method is an effective instrument for viewing the molecular complex and structures as well as chemical bonding in the excited state of quercetin-copper ion complexes. As reported in the literature, using UV-vis spectrophotometry, quercetin shows band I absorption (~300 - 380 nm), and band II absorption (240 - 280 nm). Upon the reaction

with copper ion with ratio formation of 1:1, it is observed the shifting peak from 370 nm to about 450 nm upon increased copper ion concentration. [70,71] Here, we propose to use Si-NW field effect transistor (bio-NW FET) device to study molecular absorption change and detect the different concentration of copper in the quercetin-metal complexes.

According to reports, the bio-NW FET technology provides an effective platform for detecting interactions between biomolecules [72,73], but less is known about its ability to be combined with the optoelectronic function of FET to create dual-function sensing devices. [74]. These devices have the distinct advantages of semiconductor device technology for mass production, miniaturization, low power consumption, and ease of integration [73]. In our previous study [18], using ELISA technology, we combined the charge sensing and optical transduction functions of bio-NW FETs for the detection of antibody-antigen interactions. In this work, we utilized quercetin and copper ion as the molecules for our study. Silicon has an absorption range from ultraviolet to visible wavelengths due to its high bandgap energy of 1.1 eV. In order to find the optimal and linearity for copper detection based on ion and quercetin interaction, we evaluated the effect of internal parameters (back-gate voltage and drain voltage) and external factors (wavelength and intensity) to the charge carrier. We provide a measurement of the interaction between quercetin and copper based on these variables. Additionally, the UV-vis spectrophotometric data were compared to the absorption values measured in bio-FET in various PBS solutions of 0.01X, 0.1X, and 1X.

The concentration of quercetin stock solution was 1 mM, prepared in methanol solution, and diluted to 100 μ M with PBS solution. A 100 μ M quercetin solution was added to 0.1, 0.5, 1, 10, 20, 40, 80, and 100 μ M copper chloride (CuCl_2), respectively, and reacted in 1X PBS solution for a period of time. The spectra were obtained on a commercial optical density (OD) spectrometer (JASCO V670). In our opto-FET, the measurements were conducted in the system over several on/off cycle for each concentration of CuCl_2 .

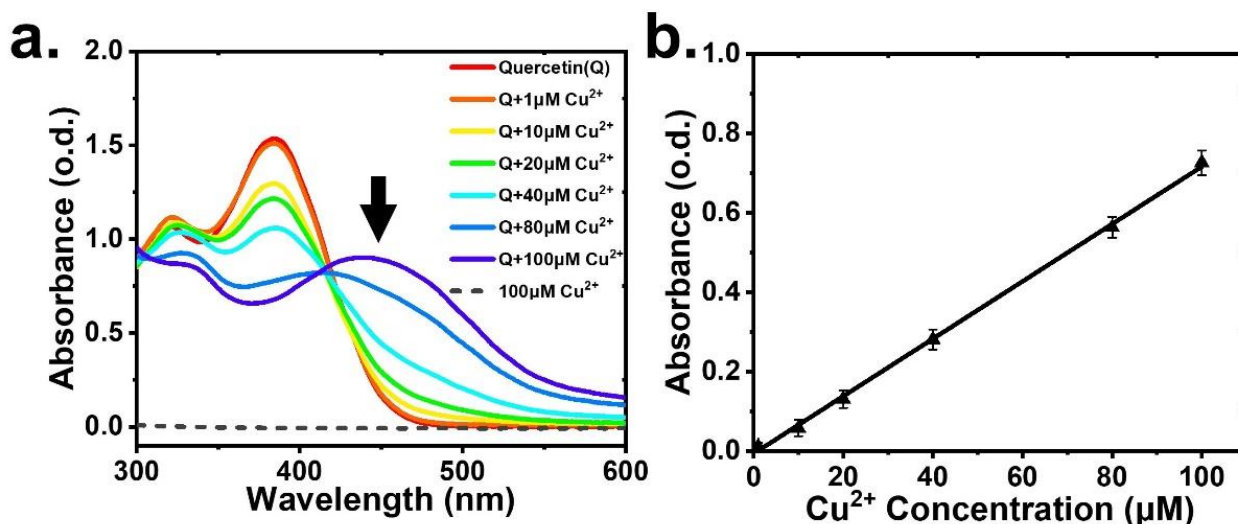


Figure 4.14. (a) UV-Vis absorption spectra of quercetin and various concentrations of Cu^{2+} in 1X PBS showing two peaks at 380 nm and 450 nm, and (b) the absorbance as a function of Cu^{2+} concentration at 450 nm.

We examined the quercetin and Cu^{2+} ion complexes in a 1X PBS solution using a commercial spectrometer (JASCO V670) with a wavelength range from 300 nm to 600 nm. As shown in **Figure 4.14a**, the results displayed the absorption peak for quercetin appeared at 385 nm and no apparent absorption peak for 100 μM of Cu^{2+} only. Upon combining quercetin with varying concentrations of Cu^{2+} solution was combined, two wavelengths were observed, 385 nm and 450 nm. With increasing Cu^{2+} concentration from 1 μM to 100 μM , the absorbance peak 385 nm wavelength was decreased and even vanished. However, the absorbance at 450 nm wavelength was increased and start to formed a peak at a quercetin with Cu^{2+} concentration of 100 μM . **Figure 4.14b** demonstrates that the absorbance at a wavelength of 450 nm linearly increased with the Cu^{2+} concentration and the solution color of the quercetin- Cu^{2+} complex in 1X PBS buffer changed from transparent (colorless) to yellowish, as shown in **Figure 4.15**.

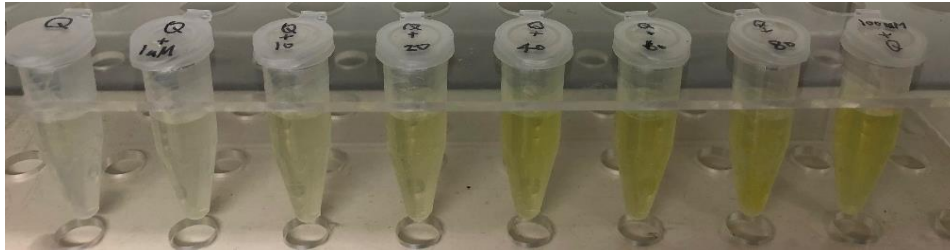


Figure 4.15. The visual change of quercetin and Cu^{2+} complexes. The pure quercetin (left) followed by mixing of quercetin and different Cu^{2+} concentrations ranging from 1 to 100 μM .

Because the quercetin– Cu^{2+} complex exhibits linear and strong absorption at wavelengths ranging from 430 to 450 nm, a wavelength of 450 nm was chosen for this study. For applications in biosensing to detect this metal complexes, we utilized the opto-FET device as a photodetector. We setup the measurement using sensor assembly with fluidic channel for opto-FET configuration as illustrated in **Figure 3.5b**, where the sample solution is not exposed to the sensing area. The Si-NW only exposed to the light to measure the molecular absorption. A suitable bias condition must be determined, wherein the detection has good sensitivity and shows a linear dependence on light intensity. This linear dependence would allow for the calibration of the molecule concentration. To this end, we measured the device by varying VDS and VBG at a wavelength of 450 nm under different light intensities, and the results are shown in **Figure 4.16a**. The graph shows that increasing the VDS value increased the photocurrent of the device. However, for different VDS values, the maximum photocurrent appeared at different VBG values in the range of 2–4 V. We limited the light intensity to 1000 nWcm^{-2} , as intense light could harm the molecules. **Figure 4.16b** shows the intensity dependence of the photocurrent for the five VDS values used in **Figure 4.16a**; in addition, the VBG values corresponded to the maximum photocurrent at 1000 nWcm^{-2} for each VDS trace. The plot shows that the optimal bias condition for this opto-FET was VDS at 0.5 V and VBG at 2.8 V.

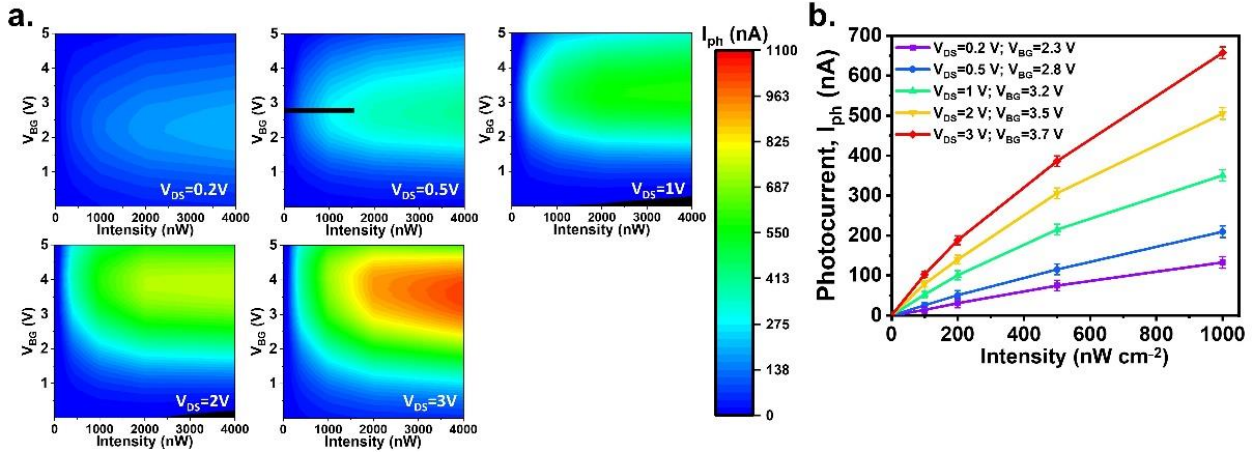


Figure 4.16. (a) The photocurrent at a wavelength of 450 nm plotted as functions of VBG and light intensities, for VDS at 0.2 V, 0.5 V, 1 V, 2 V, and 3 V. The color scale bar is shown on the right. (b) The photocurrent as a function of light intensity. It shows a linear dependence at VDS = 0.5 V and VBG = 2.8 V.

To demonstrate the use of the opto-FET device for detecting the quercetin-Cu²⁺ complex, we set the light intensity to 500 nWcm². Prior to being injected into the opto-FET fluidic channel, the solutions were first combined in a tube. The realtime measurements were performed over several on/off cycles controlled by a light shutter. **Figure 4.17** depicts the results of testing different Cu²⁺ concentrations ranging from 0.1 μM to 100 μM at various PBS concentrations for quantitative evaluation. Quercetin was used as the control experiment, as it could absorb 450 nm photons. As predicted, the photoabsorption current increased with increasing of Cu²⁺ concentration.

The relationship between the absorbance A and the concentration of an absorbing molecules can be described by the Beer–Lambert law [22]:

$$A = -\log\left(\frac{I}{I_0}\right) = \epsilon \cdot l \cdot c \quad (4.4)$$

where I_0 and I represent the initial light intensity and the light intensity after passing through the solution, respectively, ϵ represents the molar absorptivity with the unit of $\text{L mol}^{-1} \cdot \text{cm}^{-1}$, l represents the photon path length with the unit of cm, and c represents the concentration of an

absorbing molecule in the units of $\text{mol}\cdot\text{cm}^{-1}$. According to the equation, the number of molecules in the radiation path increases with the length of the path, increasing the absorbance. The absorbance is directly proportional to the analyte concentration for a given path length. This relationship allowed for the quantification of the concentration of absorbing molecules. Using equation (4.4), we can calculate the absorbance of the sample molecule.

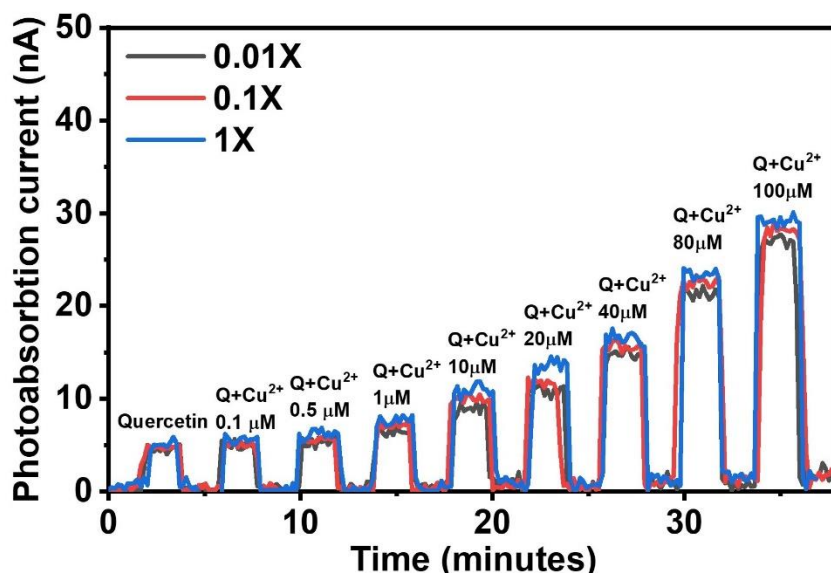


Figure 4.17. Absorption measurement of quercetin– Cu^{2+} ion mixture for various Cu^{2+} concentrations ranging from $0.1 \mu\text{M}$ to $100 \mu\text{M}$ in three different concentrations of PBS solution. A $100 \mu\text{M}$ quercetin was used as a control sample.

As shown in **Figure 4.16** shows that at a light intensity of 500 nWcm^2 , the transmittance photocurrent (I_0) was approximately 100 nA . The photoabsorption current ($I_0 - I$) was obtained after passing through the solution. Together, we obtained the absorbance of the quercetin– Cu^{2+} complexes, as shown in **Figure 4.18**. The different buffer solutions affected the wavelength during the quercetin– Cu^{2+} ion activity. Further, the absorption at a wavelength of 450 nm decreased as the buffer concentration decreased due to changes in pH value when the buffer solution was diluted. As reported in the literature [5], pH affects absorption because protons are released when the buffer forms a complex with metal ions.

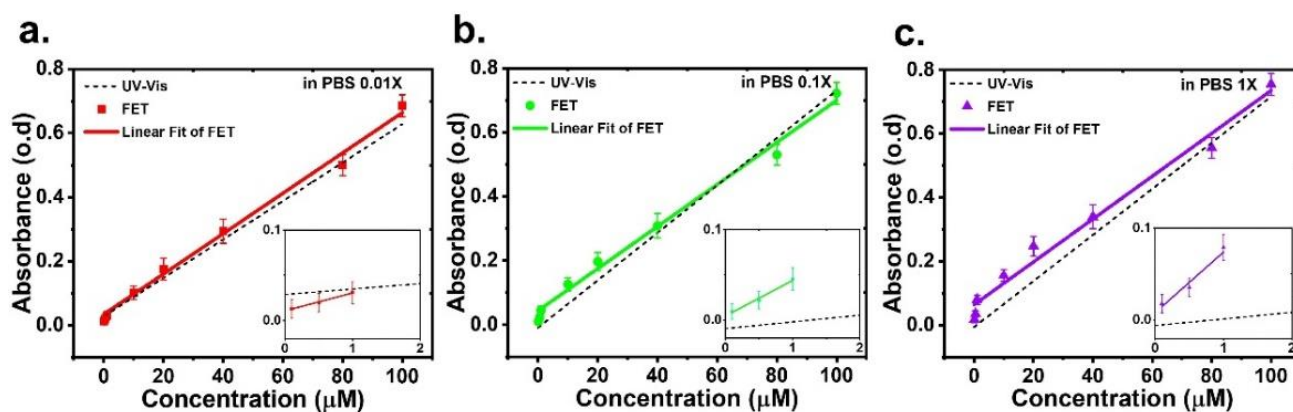


Figure 4.18. A comparison between the absorbance achieved with a commercial UV-Vis spectrometer (dot-dashed lines) and our opto-FET system (solid lines) in (a) 0.01X (b) 0.1X, and (c) 1X PBS concentration. The evaluation was performed in VDS at 0.5 V, VBG at 2.8 V, a wavelength of 450 nm, and light intensity at 500 nWcm^{-2} .

As described in the fluidic channel in chapter 3, the thickness of the fluidic channel in our system was 1.6 mm, which denotes as the path length of the sample. In comparison to a commercial UV-Vis spectrometer, which has a path length of about 10 mm, the sample measured in our system was about 6.25 times smaller. The magnitude of absorbance in our system was magnified by 6.25 times for comparison with a commercial UV-Vis sensor and our opto-FET sensor. We plotted the absorbance as a function of Cu^{2+} concentration, along with the absorbance results obtained using a commercial UV-Vis spectrometer in various buffer solutions, as shown in **Figure 4.18**. With the fluidic channel design, the amount of solution used in the opto-FET system was significantly less compared with that used in the UV-Vis system. Our fluidic system is normally capable of handling low sample volumes of about 14.1 μL , but it also has a short time to increase sensitivity and accuracy. The opto-FET photodetector can therefore be integrated into current bio-NW FET sensors thanks to its advantages, turning them into dual-function platforms for biomolecule detection.

Chapter 5 Conclusions

In conclusion, the integration of electrical and optical functions of bio-FETs greatly enhances the capabilities of present-day FET-based molecular sensors. We demonstrated a good photoresponse in a broad wavelength which is applicable for optical function ranging between 400 nm and 1000 nm. Thus, facilitating the detection of NGAL through oxidized TMB which exhibits molecular absorption as well as the quercetin-Cu²⁺ complexes.

When used as a charge sensor, it owns high detection sensitivity due to the inherent high charge-sensitive character of bio-FETs. When used as a photosensor, it enjoys label-free detection getting around stringent surface modification required by bio-FET. For quantitative detection of NGAL, we achieved a sensitivity of 0.1 pg/mL when bio-FET was used as a charge sensor and < 1 pg/mL when used as a photosensor.

The molecular absorption of the quercetin-Cu²⁺ complex was adopted as the basis for biomedical application in our system. Detection of the molecular absorption of metal complexes was performed for Cu²⁺ concentrations ranging from 0.1 μM to 100 μM, and the system exhibited a linearity and sensitivity detection of 0.1 μM Cu²⁺. The measured absorbance was compared with that obtained from a commercial UV-Vis spectrometer.

The opto-FET system offers significant potential for the biotechnology and healthcare industries as an optical biosensing device with high detection capability, high reproducibility, and low sample volume requirements. Moreover, these features of electro-optical bio-FET sensor make it an excellent candidate for lab-on-chip integration which provides rapid, simple, and high sensitivity information for miscellaneous molecule detection.

References

1. Chen, K.-I.; Li, B.-R.; Chen, Y.-T. Silicon nanowire field-effect transistor-based biosensors for biomedical diagnosis and cellular recording investigation. *Nano Today* **2011**, *6*, 131-154.
2. Baraban, L.; Ibarlucea, B.; Baek, E.; Cuniberti, G. Hybrid silicon nanowire devices and their functional diversity. *Adv Sci (Weinh)* **2019**, *6*, 1900522.
3. Seo, G.; Lee, G.; Kim, M.J.; Baek, S.H.; Choi, M.; Ku, K.B.; Lee, C.S.; Jun, S.; Park, D.; Kim, H.G., *et al.* Rapid detection of covid-19 causative virus (sars-cov-2) in human nasopharyngeal swab specimens using field-effect transistor-based biosensor. *ACS Nano* **2020**, *14*, 5135-5142.
4. Pritiraj Mohantya, Y.C., Xihua Wanga, Mi K. Honga, Carol L. Rosenbergb, David T. Weaver, Shyamsunder Erramillia. Field effect transistor nanosensor for breast cancer diagnostics. **2014**.
5. Chu, C.J.; Yeh, C.S.; Liao, C.K.; Tsai, L.C.; Huang, C.M.; Lin, H.Y.; Shyue, J.J.; Chen, Y.T.; Chen, C.D. Improving nanowire sensing capability by electrical field alignment of surface probing molecules. *Nano letters* **2013**, *13*, 2564-2569.
6. Lorenzelli, L.; Margesin, B.; Martinoia, S.; Tedesco, M.T.; Valle, M. Bioelectrochemical signal monitoring of in-vitro cultured cells by means of an automated microsystem based on solid state sensor-array. *Biosensors and Bioelectronics* **2003**, *18*, 621-626.
7. Martinoia, S.; Rosso, N.; Grattarola, M.; Lorenzelli, L.; Margesin, B.; Zen, M. Development of isfet array-based microsystems for bioelectrochemical measurements of cell populations. *Biosensors and Bioelectronics* **2001**, *16*, 1043-1050.
8. Yang, F.; Zhang, G.-J. Silicon nanowire-transistor biosensor for study of molecule-molecule interactions. *Reviews in Analytical Chemistry* **2014**, *33*.
9. Duan, X.; Li, Y.; Rajan, N.K.; Routenberg, D.A.; Modis, Y.; Reed, M.A. Quantification of the affinities and kinetics of protein interactions using silicon nanowire biosensors. *Nat Nanotechnol* **2012**, *7*, 401-407.
10. Ibarlucea, B.; Rim, T.; Baek, C.K.; de Visser, J.; Baraban, L.; Cuniberti, G. Nanowire sensors monitor bacterial growth kinetics and response to antibiotics. *Lab Chip* **2017**, *17*, 4283-4293.
11. Vacic, A.; Criscione, J.M.; Rajan, N.K.; Stern, E.; Fahmy, T.M.; Reed, M.A. Determination of molecular configuration by debye length modulation. *J Am Chem Soc* **2011**, *133*, 13886-13889.
12. Zhang, A.; Lieber, C.M. Nano-bioelectronics. *Chem Rev* **2016**, *116*, 215-257.

13. Chu, C.H.; Sarangadharan, I.; Regmi, A.; Chen, Y.W.; Hsu, C.P.; Chang, W.H.; Lee, G.Y.; Chyi, J.I.; Chen, C.C.; Shiesh, S.C., *et al.* Beyond the debye length in high ionic strength solution: Direct protein detection with field-effect transistors (fets) in human serum. *Sci Rep* **2017**, *7*, 5256.
14. Nakatsuka, N.; Yang, K.-A.; Abendroth, J.M.; Cheung, K.M.; Xu, X.; Yang, H.; Zhao, C.; Zhu, B.; Rim, Y.S.; Yang, Y., *et al.* Aptamer–field-effect transistors overcome debye length limitations for small-molecule sensing. *Science* **2018**, *362*, 319-324.
15. Tarasov, A.; Wipf, M.; Stoop, R.L.; Bedner, K.; Fu, W.; Guzenko, V.A.; Knopfmacher, O.; Calame, M.; Schönenberger, C. Understanding the electrolyte background for biochemical sensing with ion-sensitive field-effect transistors. *ACS Nano* **2012**, *6*, 9291-9298.
16. Lin, S.-P.; Pan, C.-Y.; Tseng, K.-C.; Lin, M.-C.; Chen, C.-D.; Tsai, C.-C.; Yu, S.-H.; Sun, Y.-C.; Lin, T.-W.; Chen, Y.-T. A reversible surface functionalized nanowire transistor to study protein–protein interactions. *Nano Today* **2009**, *4*, 235-243.
17. Baek, E.; Pregl, S.; Shaygan, M.; Römhildt, L.; Weber, W.M.; Mikolajick, T.; Ryndyk, D.A.; Baraban, L.; Cuniberti, G. Optoelectronic switching of nanowire-based hybrid organic/oxide/semiconductor field-effect transistors. *Nano Research* **2014**, *8*, 1229-1240.
18. Laksana, P.J.B.; Tsai, L.-C.; Wei, T.-Y.; Lan, P.-C.; Chang-Liao, K.-S.; Moodley, M.K.; Chen, C.-D. A dual function electro-optical silicon field-effect transistor molecular sensor. *Journal of Materials Chemistry C* **2021**, *9*, 14286-14293.
19. Makris, K.; Markou, N.; Evodia, E.; Dimopoulou, E.; Drakopoulos, I.; Ntetsika, K.; Rizos, D.; Baltopoulos, G.; Haliassos, A. Urinary neutrophil gelatinase-associated lipocalin (ngal) as an early marker of acute kidney injury in critically ill multiple trauma patients. *Clin Chem Lab Med* **2009**, *47*, 79-82.
20. Laksana, P.J.B.; Tsai, L.-C.; Lin, C.-C.; Chang-Liao, K.-S.; Moodley, M.K.; Chen, C.-D. Opto field-effect transistors for detecting quercetin–cu²⁺ complex. *Sensors* **2022**, *22*, 7219.
21. Nagel, B.; Dellweg, H.; Gierasch, L.M. Glossary for chemists of terms used in biotechnology (iupac recommendations 1992). *Pure and Applied Chemistry* **1992**, *64*, 143-168.
22. Udugama, B.; Kadhiresan, P.; Kozlowski, H.N.; Malekjahani, A.; Osborne, M.; Li, V.Y.C.; Chen, H.; Mubareka, S.; Gubbay, J.B.; Chan, W.C.W. Diagnosing covid-19: The disease and tools for detection. *ACS Nano* **2020**, *14*, 3822-3835.
23. Xiaoyan Zhanga, d., Qige Qia, Qiushi Jinga, Shen Aoa,b, Zhihong Zhange, Mingchao Dingc, Muhong Wuc, Kaihui Liuc, Weipeng Wangb, Yunhan Lingb, Zhengjun Zhangb, Wangyang Fua,b,* .Electrical probing of covid-19 spike protein receptor binding domain via a graphene field effect transistor. **2020**.

24. Koike, K.; Sasaki, T.; Hiraki, K.; Ike, K.; Hirofuji, Y.; Yano, M. Characteristics of an extended gate field-effect transistor for glucose sensing using an enzyme-containing silk fibroin membrane as the bio-chemical component. *Biosensors* **2020**, *10*, 57.
25. Council, N.R. *Expanding the vision of sensor materials*. The National Academies Press: Washington, DC, 1995; p 146.
26. Rani, D.; Pachauri, V.; Madaboosi, N.; Jolly, P.; Vu, X.-T.; Estrela, P.; Chu, V.; Conde, J.P.; Ingebrandt, S. Top-down fabricated silicon nanowire arrays for field-effect detection of prostate-specific antigen. *ACS Omega* **2018**, *3*, 8471-8482.
27. Arjmand, T.; Legallais, M.; Nguyen, T.T.T.; Serre, P.; Vallejo-Perez, M.; Morisot, F.; Salem, B.; Ternon, C. Functional devices from bottom-up silicon nanowires: A review. *Nanomaterials* **2022**, *12*, 1043.
28. Gao, X.P.A.; Zheng, G.; Lieber, C.M. Subthreshold regime has the optimal sensitivity for nanowire fet biosensors. *Nano letters* **2010**, *10*, 547-552.
29. Cui, Y.; Zhong, Z.; Wang, D.; Wang, W.U.; Lieber, C.M. High performance silicon nanowire field effect transistors. *Nano letters* **2003**, *3*, 149-152.
30. Penner, R.M. Chemical sensing with nanowires. *Annual Review of Analytical Chemistry* **2012**, *5*, 461-485.
31. Shehada, N.; Cancilla, J.C.; Torrecilla, J.S.; Pariente, E.S.; Bronstrup, G.; Christiansen, S.; Johnson, D.W.; Leja, M.; Davies, M.P.; Liran, O., *et al.* Silicon nanowire sensors enable diagnosis of patients via exhaled breath. *ACS Nano* **2016**, *10*, 7047-7057.
32. Waleed Shinwari, M.; Jamal Deen, M.; Landheer, D. Study of the electrolyte-insulator-semiconductor field-effect transistor (eisfet) with applications in biosensor design. *Microelectronics Reliability* **2007**, *47*, 2025-2057.
33. Cui, Y.; Lieber, C.M. Functional nanoscale electronic devices assembled using silicon nanowire building blocks. *Science* **2001**, *291*, 851-853.
34. Sinha, S.; Pal, T. A comprehensive review of fet-based ph sensors: Materials, fabrication technologies, and modeling. *Electrochemical Science Advances* **2022**, *2*, e2100147.
35. Sorgenfrei, S.; Chiu, C.-y.; Johnston, M.; Nuckolls, C.; Shepard, K.L. Debye screening in single-molecule carbon nanotube field-effect sensors. *Nano letters* **2011**, *11*, 3739-3743.
36. Stern, E.; Wagner, R.; Sigworth, F.J.; Breaker, R.; Fahmy, T.M.; Reed, M.A. Importance of the debye screening length on nanowire field effect transistor sensors. *Nano letters* **2007**, *7*, 3405-3409.

37. Howarter, J.A.; Youngblood, J.P. Surface modification of polymers with 3-aminopropyltriethoxysilane as a general pretreatment for controlled wettability. *Macromolecules* **2007**, *40*, 1128-1132.
38. Pursch, M.; Vanderhart, D.L.; Sander, L.C.; Gu, X.; Nguyen, T.; Wise, S.A.; Gajewski, D.A. C30 self-assembled monolayers on silica, titania, and zirconia: Hplc performance, atomic force microscopy, ellipsometry, and nmr studies of molecular dynamics and uniformity of coverage. *Journal of the American Chemical Society* **2000**, *122*, 6997-7011.
39. Xiang, J.; Zhu, P.; Masuda, Y.; Koumoto, K. Fabrication of self-assembled monolayers (sams) and inorganic micropattern on flexible polymer substrate. *Langmuir* **2004**, *20*, 3278-3283.
40. Fadeev, A.Y.; McCarthy, T.J. Self-assembly is not the only reaction possible between alkyltrichlorosilanes and surfaces: Monomolecular and oligomeric covalently attached layers of dichloro- and trichloroalkylsilanes on silicon. *Langmuir* **2000**, *16*, 7268-7274.
41. Engvall, E.; Perlmann, P. Enzyme-linked immunosorbent assay (elisa) quantitative assay of immunoglobulin g. *Immunochemistry* **1971**, *8*, 871-874.
42. Thiha, A.; Ibrahim, F. A colorimetric enzyme-linked immunosorbent assay (elisa) detection platform for a point-of-care dengue detection system on a lab-on-compact-disc. *Sensors* **2015**, *15*, 11431-11441.
43. Cerda-Kipper, A.S.; Montiel, B.E.; Hosseini, S. Immunoassays | radioimmunoassays and enzyme-linked immunosorbent assay☆. In *Encyclopedia of analytical science (third edition)*, Worsfold, P.; Poole, C.; Townshend, A.; Miró, M., Eds. Academic Press: Oxford, 2019; pp 55-75.
44. Voller, A.; Bartlett, A.; Bidwell, D.E. Enzyme immunoassays with special reference to elisa techniques. *Journal of Clinical Pathology* **1978**, *31*, 507.
45. Hosoda, H.; Takasaki, W.; Oe, T.; Tsukamoto, R.; Nambara, T. A comparison of chromogenic substrates for horseradish peroxidase as a label in steroid enzyme immunoassay. *CHEMICAL & PHARMACEUTICAL BULLETIN* **1986**, *34*, 4177-4182.
46. Porstmann, B.; Porstmann, T.; Nugel, E. Comparison of chromogens for the determination of horseradish peroxidase as a marker in enzyme immunoassay. **1981**, *19*, 435-440.
47. Soni, S.S.; Cruz, D.; Bobek, I.; Chionh, C.Y.; Nalesso, F.; Lentini, P.; de Cal, M.; Corradi, V.; Virzi, G.; Ronco, C. Ngal: A biomarker of acute kidney injury and other systemic conditions. *International Urology and Nephrology* **2010**, *42*, 141-150.

48. Forster, C.S.; Johnson, K.; Patel, V.; Wax, R.; Rodig, N.; Barasch, J.; Bachur, R.; Lee, R.S. Urinary ngal deficiency in recurrent urinary tract infections. *Pediatr Nephrol* **2017**, *32*, 1077-1080.
49. Sariki, A.; Venkata Rao, K.; Chandrasekar, L.; Shaik, R.R.; Pradhan, K.P. Is accumulation or inversion mode dielectric modulated fet better for label-free biosensing?: A comparative investigation. *AEU - International Journal of Electronics and Communications* **2021**, *137*, 153791.
50. Sheng-Lyang Jang *, S.-S.L. A novel approach for modeling accumulation-mode soi mosfets. **1998**
51. Baek, D.J.; Duarte, J.P.; Moon, D.-I.; Kim, C.-H.; Ahn, J.-H.; Choi, Y.-K. Accumulation mode field-effect transistors for improved sensitivity in nanowire-based biosensors. *Applied Physics Letters* **2012**, *100*, 213703.
52. Baek, E.; Rim, T.; Schutt, J.; Baek, C.K.; Kim, K.; Baraban, L.; Cuniberti, G. Negative photoconductance in heavily doped si nanowire field-effect transistors. *Nano letters* **2017**, *17*, 6727-6734.
53. Moniaux, N.; Chakraborty, S.; Yalniz, M.; Gonzalez, J.; Shostrom, V.K.; Standop, J.; Lele, S.M.; Ouellette, M.; Pour, P.M.; Sasson, A.R., *et al.* Early diagnosis of pancreatic cancer: Neutrophil gelatinase-associated lipocalin as a marker of pancreatic intraepithelial neoplasia. *Br J Cancer* **2008**, *98*, 1540-1547.
54. Helle, M.; Boeije, L.; de Groot, E.; de Vos, A.; Aarden, L. Sensitive elisa for interleukin-6: Detection of il-6 in biological fluids: Synovial fluids and sera. *Journal of Immunological Methods* **1991**, *138*, 47-56.
55. Vashist, S.K.; Marion Schneider, E.; Lam, E.; Hrapovic, S.; Luong, J.H. One-step antibody immobilization-based rapid and highly-sensitive sandwich elisa procedure for potential in vitro diagnostics. *Sci Rep* **2014**, *4*, 4407.
56. Kannan, P.; Tiong, H.Y.; Kim, D.H. Highly sensitive electrochemical determination of neutrophil gelatinase-associated lipocalin for acute kidney injury. *Biosens Bioelectron* **2012**, *31*, 32-36.
57. Vashist, S.K. Graphene-based immunoassay for human lipocalin-2. *Anal Biochem* **2014**, *446*, 96-101.
58. Vashist, S.K.; Luong, J.H.T. A rapid and highly sensitive immunoassay format for human lipocalin-2 using multiwalled carbon nanotubes. *Biosens Bioelectron* **2017**, *93*, 198-204.
59. Yukird, J.; Wongtangprasert, T.; Rangkupan, R.; Chailapakul, O.; Pisitkun, T.; Rodthongkum, N. Label-free immunosensor based on graphene/polyaniline nanocomposite for neutrophil gelatinase-associated lipocalin detection. *Biosens Bioelectron* **2017**, *87*, 249-255.

60. World Health, O.; International Atomic Energy, A.; Food; Agriculture Organization of the United, N. Trace elements in human nutrition and health. World Health Organization: Geneva, 1996.
61. Liu, Y.; Guo, M. Studies on transition metal-quercetin complexes using electrospray ionization tandem mass spectrometry. *Molecules* **2015**, *20*, 8583-8594.
62. Jiang, W.; Yang, S.; Lu, W.; Gao, B.; Xu, L.; Sun, X.; Jiang, D.; Xu, H.-J.; Ma, M.; Cao, F. A novel fluorescence “turn off-on” nano-sensor for detecting cu²⁺ and cysteine in living cells. *Journal of Photochemistry and Photobiology A: Chemistry* **2018**, *362*, 14-20.
63. da Silva, W.M.B.; de Oliveira Pinheiro, S.; Alves, D.R.; de Menezes, J.; Magalhaes, F.E.A.; Silva, F.C.O.; Silva, J.; Marinho, E.S.; de Moraes, S.M. Synthesis of quercetin-metal complexes, in vitro and in silico anticholinesterase and antioxidant evaluation, and in vivo toxicological and anxiolytic activities. *Neurotox Res* **2020**, *37*, 893-903.
64. Zhang, L.; Liu, Y.; Wang, Y.; Xu, M.; Hu, X. Uv-vis spectroscopy combined with chemometric study on the interactions of three dietary flavonoids with copper ions. *Food Chem* **2018**, *263*, 208-215.
65. Pekal, A.; Biesaga, M.; Pyrzynska, K. Interaction of quercetin with copper ions: Complexation, oxidation and reactivity towards radicals. *Biometals* **2011**, *24*, 41-49.
66. Tapiero, H.; Townsend, D.M.; Tew, K.D. Trace elements in human physiology and pathology. Copper. *Biomed Pharmacother* **2003**, *57*, 386-398.
67. Kalinowska, M.; Lewandowska, H.; Pruszyński, M.; Świdorski, G.; Gołębiewska, E.; Gryko, K.; Braun, J.; Borkowska, M.; Konieczna, M.; Lewandowski, W. Co(ii) complex of quercetin–spectral, anti-/pro-oxidant and cytotoxic activity in hacat cell lines. *Applied Sciences* **2021**, *11*, 9244.
68. Malesev, D.; Kuntic, V. Investigation of metal-flavonoid chelates and the determination of flavonoids via metal-flavonoid complexing reactions. *Journal of the Serbian Chemical Society* **2007**, *72*, 921-939.
69. Ravichandran, R.; Rajendran, M.; Devapiriam, D. Antioxidant study of quercetin and their metal complex and determination of stability constant by spectrophotometry method. *Food Chem* **2014**, *146*, 472-478.
70. de Castilho, T.S.; Matias, T.B.; Nicolini, K.P.; Nicolini, J. Study of interaction between metal ions and quercetin. *Food Science and Human Wellness* **2018**, *7*, 215-219.
71. Lewis, T.; Wallace, W.; Peterson, F.D.; Rafferty, S.; Martic, S. Reactivities of quercetin and metallo-quercetin with superoxide anion radical and molecular oxygen. *Electrochemical Science Advances* **2021**, *2*.

72. Dai, P.; Gao, A.; Lu, N.; Li, T.; Wang, Y. A back-gate controlled silicon nanowire sensor with sensitivity improvement for DNA and ph detection. *Japanese Journal of Applied Physics* **2013**, *52*, 121301.
73. Wu, T.; Alharbi, A.; You, K.D.; Kisslinger, K.; Stach, E.A.; Shahrjerdi, D. Experimental study of the detection limit in dual-gate biosensors using ultrathin silicon transistors. *ACS Nano* **2017**, *11*, 7142-7147.
74. Alharbi, A.G.; Shafi, N. Liquid gate and back gate capacitive coupling effects in ph sensing performance of finfets. *Silicon* **2022**.



Appendix A

List of publications.

Article include in this dissertation:

1. Laksana, P.J.B.; Tsai, L.-C.; Wei, T.-Y.; Lan, P.-C.; Chang-Liao, K.-S.; Moodley, M.K.; Chen, C.-D. A dual function electro-optical silicon field-effect transistor molecular sensor. *Journal of Materials Chemistry C* **2021**, *9*, 14286-14293.
2. Laksana, P.J.B.; Tsai, L.-C.; Lin, C.-C.; Chang-Liao, K.-S.; Moodley, M.K.; Chen, C.-D. Opto field-effect transistors for detecting quercetin–cu²⁺ complex. *Sensors* **2022**, *22*, 7219.
3. ChiiDong, Chen., Pradhana Jati Budhi Laksana, and Chu Chia-Jung. "Dual function electro-optical silicon field-effect transistor molecular sensor." U.S. Patent Application 17/542,822, filed June 9, 2022.

